

# Neuronal vulnerability and multilineage diversity in multiple sclerosis

Lucas Schirmer<sup>1,2,3,4,13</sup>, Dmitry Velmeshev<sup>1,5,13</sup>, Staffan Holmqvist<sup>2</sup>, Max Kaufmann<sup>6</sup>, Sebastian Werneburg<sup>7</sup>, Diane Jung<sup>1,5</sup>, Stephanie Vistnes<sup>1,4</sup>, John H. Stockley<sup>2</sup>, Adam Young<sup>8,9</sup>, Maïke Steindel<sup>2</sup>, Brian Tung<sup>1,5,10</sup>, Nitasha Goyal<sup>1,5,10</sup>, Aparna Bhaduri<sup>1,5</sup>, Simone Mayer<sup>1,5</sup>, Jan Broder Engler<sup>6</sup>, Omer A. Bayraktar<sup>2</sup>, Robin J. M. Franklin<sup>8,9</sup>, Maximilian Haeussler<sup>11</sup>, Richard Reynolds<sup>12</sup>, Dorothy P. Schafer<sup>7</sup>, Manuel A. Friese<sup>6</sup>, Lawrence R. Shiow<sup>1,4</sup>, Arnold R. Kriegstein<sup>1,5\*</sup> & David H. Rowitch<sup>1,2,4\*</sup>

**Multiple sclerosis (MS) is a neuroinflammatory disease with a relapsing–remitting disease course at early stages, distinct lesion characteristics in cortical grey versus subcortical white matter and neurodegeneration at chronic stages. Here we used single–nucleus RNA sequencing to assess changes in expression in multiple cell lineages in MS lesions and validated the results using multiplex in situ hybridization. We found selective vulnerability and loss of excitatory CUX2–expressing projection neurons in upper–cortical layers underlying meningeal inflammation; such MS neuron populations exhibited upregulation of stress pathway genes and long non–coding RNAs. Signatures of stressed oligodendrocytes, reactive astrocytes and activated microglia mapped most strongly to the rim of MS plaques. Notably, single–nucleus RNA sequencing identified phagocytosing microglia and/or macrophages by their ingestion and perinuclear import of myelin transcripts, confirmed by functional mouse and human culture assays. Our findings indicate lineage– and region–specific transcriptomic changes associated with selective cortical neuron damage and glial activation contributing to progression of MS lesions.**

MS is a progressive neuroinflammatory autoimmune disease that affects about 2.3 million people worldwide<sup>1</sup>. Immune-mediated cytotoxic damage to oligodendrocytes (OLs) causes demyelination and focal plaque formation<sup>2,3</sup> accompanied by progressive axonal damage in white matter (WM)<sup>4,5</sup>, and active MS plaques typically show a rim of inflammation with myelin phagocytosis. MS lesion heterogeneity in WM versus grey matter (GM) compartments suggests that the underlying pathobiology and potential for repair is likely to vary in a region-restricted manner. Cortical GM pathologies include demyelination and damage to the axon, neurite and neuron cell body<sup>6</sup>, particularly in areas underlying meningeal inflammation with plasma cell infiltration<sup>7–9</sup>. However, whether this process affects all or only a subset of cortical neurons is not well understood<sup>10</sup>. Indeed, cell-type-specific mechanisms of MS lesion progression, including scar formation with slowly expanding WM lesions<sup>11</sup> and cortical atrophy<sup>12</sup> are not well understood.

Single-cell transcriptomic techniques are well-suited for identification of cellular heterogeneity in the human brain; they have recently been applied to individual glial lineages in MS<sup>13,14</sup>. Here, we applied a multilineage approach to brain-resident populations (neurons, astrocytes, OLs and microglia) to better understand molecular, cellular and spatially restricted substrates of progressive MS pathology. We used frozen human brain samples from patients with MS and controls to perform unbiased isolation of nuclei from cortical and subcortical lesion and non-lesion areas followed by single-nucleus RNA-sequencing (snRNA-seq)<sup>13,15</sup> and in situ validation of RNA gene expression across large anatomical areas. Our results indicate that genes that are most

dysregulated in MS map to vulnerable upper-cortical-layer neurons and reactive glia at the borders of subcortical MS lesions associated with progression in MS.

## Molecular changes associated with MS pathogenesis

We used snRNA-seq to profile cortical GM and adjacent subcortical WM MS lesion areas at various stages of inflammation and demyelination, and control tissue from unaffected individuals. We established a pipeline for serial sectioning of entire tissue blocks including lesion and non-lesion GM and WM areas plus meningeal tissue. Tissue sections were screened for RNA integrity number (RIN) of >6.5. Using this criterion, 12 out of 19 MS tissue samples screened from 17 individuals with MS and 9 out of 16 samples screened from control individuals were further processed (Fig. 1a, Supplementary Table 1). Confounding variables of age, sex, postmortem interval and RIN were not significantly different between control subjects and individuals with MS ( $P > 0.1$ , Mann–Whitney  $U$ -test).

We optimized and performed unbiased isolation of nuclei using sucrose-gradient ultracentrifugation (Extended Data Fig. 1a) followed by snRNA barcoding and cDNA sequencing. After quality control filtering, snRNA-seq yielded 48,919 single-nucleus profiles (Fig. 1b, c). We normalized data and applied several independent analysis techniques. Unbiased clustering identified 22 cell clusters (Fig. 1c; note that none of the clusters comprised nuclei captured from only one individual MS or control sample). We detected a median of 1,400 genes and 2,400 transcripts per nucleus, with higher numbers detected in neuronal versus glial populations (Extended Data Fig. 1b, Supplementary Table 2).

<sup>1</sup>Eli and Edythe Broad Center of Regeneration Medicine and Stem Cell Research, University of California, San Francisco, San Francisco, CA, USA. <sup>2</sup>Department of Paediatrics and Wellcome–MRC Cambridge Stem Cell Institute, University of Cambridge, Cambridge, UK. <sup>3</sup>Department of Neurology, Medical Faculty Mannheim, University of Heidelberg, Mannheim, Germany. <sup>4</sup>Division of Neonatology, Department of Pediatrics, University of California, San Francisco, San Francisco, CA, USA. <sup>5</sup>Department of Neurology, University of California, San Francisco, San Francisco, CA, USA. <sup>6</sup>Institute of Neuroimmunology and Multiple Sclerosis, Center for Molecular Neurobiology Hamburg, University Medical Center Hamburg–Eppendorf, Hamburg, Germany. <sup>7</sup>Department of Neurobiology and the Brudnik Neuropsychiatric Institute, University of Massachusetts Medical School, Worcester, MA, USA. <sup>8</sup>Department of Clinical Neurosciences, University of Cambridge, Cambridge, UK. <sup>9</sup>Wellcome Trust–MRC Cambridge Stem Cell Institute, University of Cambridge, Cambridge, UK. <sup>10</sup>Department of Molecular and Cell Biology, University of California, Berkeley, Berkeley, CA, USA. <sup>11</sup>Genomics Institute, University of California, Santa Cruz, Santa Cruz, CA, USA. <sup>12</sup>Division of Brain Sciences, Department of Medicine, Imperial College London, London, UK. <sup>13</sup>These authors contributed equally: Lucas Schirmer, Dmitry Velmeshev. \*e-mail: arnold.kriegstein@ucsf.edu; dhr25@medschl.cam.ac.uk

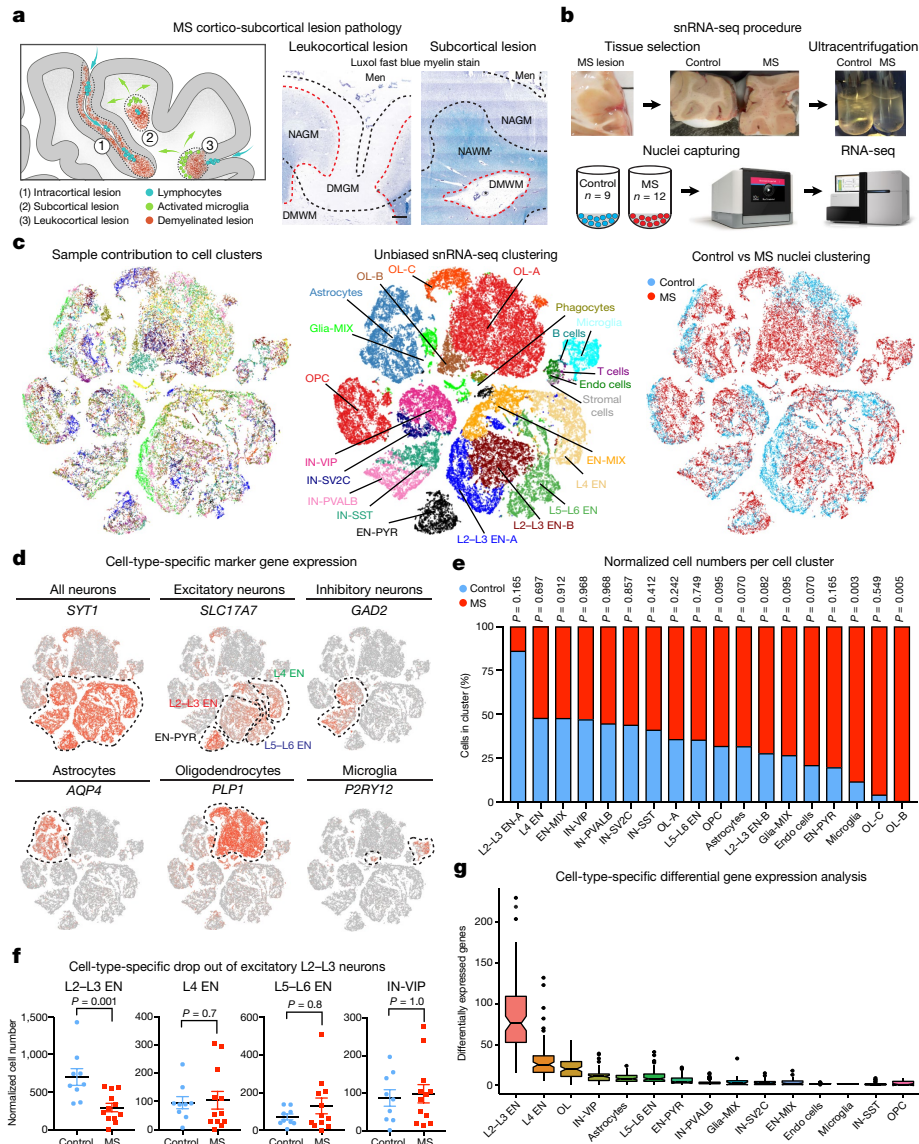


**Fig. 1 | Experimental approach and characteristics of snRNA-seq using frozen MS tissue.** **a**, Cortical and subcortical control tissue and MS lesion types. NAGM, normal-appearing grey matter; NAWM, normal-appearing white matter; DMGM, demyelinated grey matter; DMWM, demyelinated white matter; Men, meninges. Black asterisk indicates a blood vessel. Scale bar, 500  $\mu\text{m}$ . **b**, Experimental approach for isolating nuclei from postmortem snap-frozen brain samples of patients with MS and controls. **c**, Sample contribution to individual cell clusters (left), cell-type specific clusters (centre; control,  $n = 9$ ; MS,  $n = 12$ ) and control versus MS sample contribution to cell clusters (right). Note separation of L2–L3 EN and OL clusters into MS-specific clusters L2–L3 EN-B, OL-B and OL-C. Endo, endothelial. **d**,  $t$ -Distributed stochastic neighbor embedding ( $t$ -SNE) plots highlight marker genes for neurons, astrocytes, OLs and microglia. **e**, Bar chart shows contributions of normalized control and MS cell numbers to major cell-type clusters. Note that enrichment of L2–L3

Next, we annotated cell clusters on the basis of the expression of lineage marker genes for excitatory and inhibitory cortical neurons, astrocytes, OL lineage cells and microglia, as well as smaller cell populations<sup>16</sup> (Fig. 1d, Extended Data Fig. 1e, Supplementary Table 3). Neuronal-subtype markers included the excitatory neuron (EN) marker *SLC17A7*, upper-layer marker *CUX2*, layer 4 marker *RORB*, deep-layer marker *TLE4*, as well as interneuron (IN) marker *GAD2* and subtype markers *PVALB*, *SST*, *VIP* and *SV2C*. Comparing normalized numbers of nuclei from MS and control samples (Supplementary Table 4), we observed a selective reduction in numbers of ENs of the upper-layer (layer (L)2–L3; L2–L3 EN-A and L2–L3 EN-B) in MS samples with

EN-A cells and concomitant decrease in L2–L3 EN-B cells in control samples over MS was not statistically significant ( $P = 0.165$  and  $0.082$ , respectively). **f**, Specific loss of L2–L3 ENs versus L4 ENs, L5–L6 ENs or IN-VIP neurons based on normalized cell numbers. **g**, DGE analysis showing that L2–L3 ENs have the highest number of dysregulated genes, followed by L4 ENs and OL cells; the fewest differentially expressed genes were found in *SST*-expressing INs and OPCs. Box plots represent median and interquartile range (IQR) of differentially expressed gene number calculated after downsampling (100 DGE analyses per cell cluster; control,  $n = 9$ ; MS,  $n = 12$ ). Whiskers extend to the largest values within  $1.5 \times$  IQR from box boundaries, outliers are shown as dots, notches represent a 95% confidence interval around the median. Two-tailed Mann–Whitney  $U$ -tests were performed in **e** and **f** (control,  $n = 9$ ; MS,  $n = 12$ );  $*P \leq 0.05$ . Data are presented as mean  $\pm$  s.e.m. For  $t$ -SNE plots, data are shown from a total of 48,919 nuclei (control,  $n = 9$ ; MS,  $n = 12$ ).

cortical demyelination (Fig. 1e, f). By contrast, numbers of intermediate-layer (L4) ENs and deep-layer (L5–L6) ENs, high *THY1* and *NRGN*-expressing pyramidal cells, *VIP*-expressing, somatostatin (*SST*)- and parvalbumin (*PVALB*)-expressing INs were similar between MS and control samples (Fig. 1e–f). MS-associated genes showed greatest differential expression in L2–L3 ENs, followed by L4 ENs and myelinating OLs (Fig. 1g). Notably, for L2–L3 ENs and OLs, transcriptomic changes distinguished subclusters from MS or control samples (Fig. 1c, e). In contrast to L2–L3 ENs, gene dysregulation was less pronounced in upper-layer *VIP*-expressing INs (Fig. 1g). These findings suggested cell-type vulnerability of L2–L3 *CUX2*-expressing ENs.

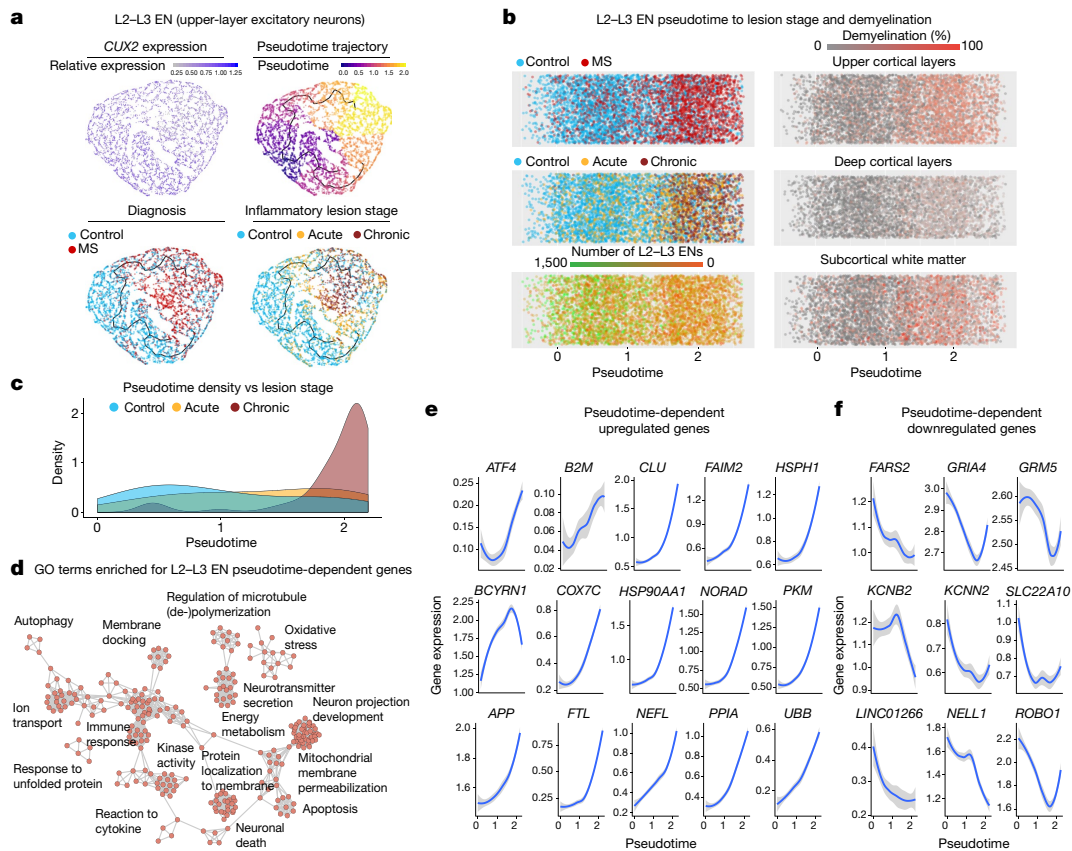


**Fig. 2 | Pseudotime trajectory analysis of upper-layer ENs.** **a**, Trajectory analysis of *CUX2*-expressing L2–L3 ENs (top left). Unsupervised pseudotime trajectories within the L2–L3 EN cluster (top right) reflect cellular origin from MS samples or controls (bottom left) and inflammatory lesion stage (bottom right). Acute, acute chronic-active; chronic, chronic inactive. **b**, L2–L3 EN pseudotime trajectories showed similar features as in **a** and suggested loss of normalized L2–L3 EN numbers (bottom left). The strongest association with L2–L3 EN trajectories was found for upper-cortical-layer demyelination (top right) versus deep-cortical-layer (middle right) and subcortical demyelination (bottom right). **c**, Note selective enrichment of dysregulated genes in

### Selective vulnerability of upper-layer neurons in MS

We investigated changes in *CUX2*-expressing L2–L3 ENs in MS lesion pathology using unsupervised pseudotime trajectory analysis to identify dynamic gene expression changes. As shown in Fig. 2a, the cell distribution along the trajectory separated control from MS specimens in L2–L3 ENs. Of note, progression along the trajectory correlated with conventional inflammatory lesion staging and the degree of upper-layer cortical demyelination (Fig. 2b, Extended Data Fig. 1c, d). For example, *CUX2*-expressing neurons, which localized towards the trajectory end, derived predominantly from samples harbouring late chronic inactive lesions with extensive subpial demyelination versus lesions with less upper cortical demyelination (Fig. 2c).

Trajectory analysis highlighted gene ontology (GO) terms and dynamic upregulation of oxidative stress, mitochondrial dysfunction and cell death pathways in L2–L3 ENs, including *FAIM2*, *ATF4*, *CLU* and *B2M* (cell stress/death), *HSPH1* and *HSP90AA1* (heat-shock response), *APP*, *NEFL* and *UBB* (protein accumulation, axon degradation), *COX7C*, *PKM* and *PPIA* (energy metabolism, oxidative stress) and long-noncoding (lnc)RNAs *LINC00657* (also known as *NORAD*) and *BCYRN1* (also known as *BC200*)<sup>17,18</sup> (Fig. 2d, e, Extended Data Fig. 2a, Supplementary Table 5). Conversely, we noted dynamic downregulation of transcripts associated with mitochondrial energy consumption (*FARS2*), glutamate signalling (*GRIA4* and *GRM5*), potassium or cation homeostasis (*KCNB2*, *KCNN2* and *SLC22A10*), neuronal signalling (*NELL1*), axon plasticity (*ROBO1*) and lncRNA

L2–L3 EN cells from samples with late chronic inactive lesions versus acute or chronic-active and control samples. **d**, Visualization of GO terms (enrichment calculated using gene-set enrichment analysis, false discovery rate (FDR)-adjusted  $P \leq 0.05$ , no terms significantly decreased) in genes significantly regulated in L2–L3 ENs in a pseudotime-dependent manner (Moran's *I* test, FDR-adjusted  $P \leq 0.0001$ ). Note enrichment of severe cell stress processes. **e**, **f**, Trajectory-dependent upregulated (**e**) and downregulated (**f**) L2–L3 EN genes of interest. Grey shading represents 95% confidence interval based on gene expression in all ( $n = 5,938$ ) sampled L2–L3 EN nuclei.

*LINC01266* (Fig. 2f). Neurons from all cortical layers in MS showed enrichment of cell stress pathways compared to controls (Extended Data Fig. 2b, Supplementary Table 6). By contrast, *PVALB*- and *VIP*-expressing INs showed only one GO term (associated with protein folding) enriched for dysregulated genes. Together, these findings highlighted a selective transcriptomic damage signature for *CUX2*-expressing neurons in MS.

### Loss of *CUX2*-expressing neurons in MS lesions in situ

We next used large area spatial transcriptomic (LAST) mapping<sup>19</sup> to validate cell-type-specific changes in gene expression. We optimized chromogenic and multiplex small-molecule fluorescence in situ hybridization (smFISH) protocols to overcome high levels of background autofluorescence in WM and GM areas in frozen human brain samples. We achieved a favourable signal-to-noise ratio over tissue sections for neuronal markers *CUX2* and *SYT1* combined with immunohistochemistry for myelin oligodendrocyte glycoprotein (MOG), and confirmed layer-associated expression of neuronal subtype markers *RORB*, *THY1*, *TLE4*, *VIP* and *SST* (Fig. 3a–e, Extended Data Fig. 3a).

On the basis of the snRNA-seq findings described above, we investigated expression of co-located upper-layer *CUX2*- and *VIP*-expressing populations by smFISH in MS and control sections (Fig. 3f). We found a significant reduction in *CUX2*-expressing neurons in completely and incompletely demyelinated cortical areas in MS tissue; by contrast,

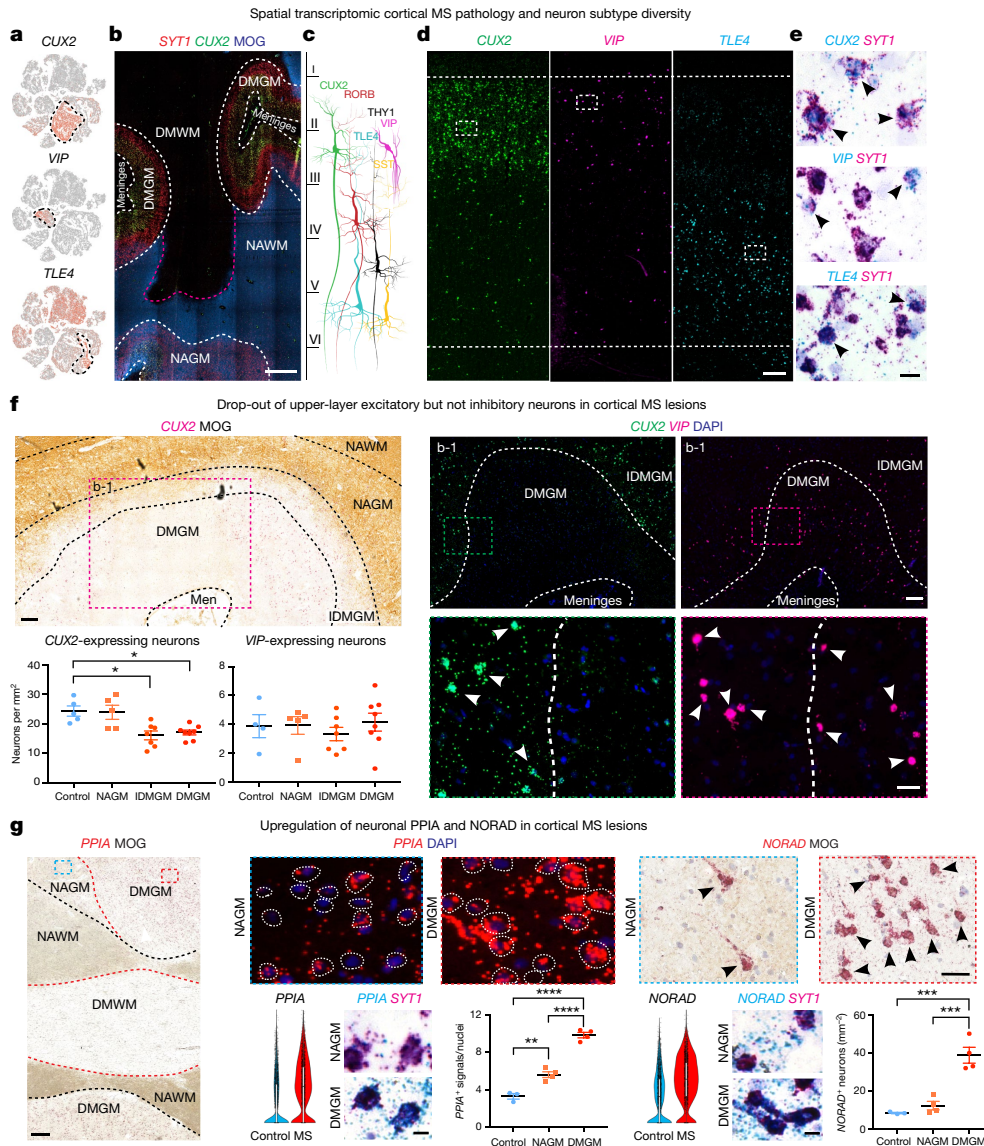


**Fig. 3 | Cellular and molecular neuronal pathology in cortical MS lesions.** **a**, *t*-SNE plots for *CUX2*, *VIP* and *TLE4*-expressing neurons (left). **b–e**, Spatial transcriptomics showing layer-specific expression of *CUX2* in lesion (indicated by loss of MOG) versus non-lesion areas (**b**). **c**, Schematic illustrates layer-specific neuron subtype diversity. **d**, smFISH, showing *CUX2* and *VIP* expression in upper and *TLE4* expression in deep-cortical layers (control,  $n = 5$ ). **e**, Validation of neuronal expression by *SYT1* in situ hybridization (black arrowheads; control,  $n = 5$ ). **f**, Right, *CUX2* and *VIP* smFISH demonstrate reduction in *CUX2*-expressing, but not *VIP*-expressing upper-layer neurons (white arrowheads) in DMGM underlying meningeal inflammation (top) versus incompletely demyelinated (IDMG), NAGM and control cortical GM (bottom left). Analysis of variance (ANOVA) with Kruskal–Wallis multiple comparison tests was performed (control,  $n = 5$  (*CUX2*),  $n = 4$  (*VIP*); MS,  $n = 8$ ;  $*P \leq 0.05$ ; different samples with NAWM, IDMG and DMGM MS

numbers of abutting *VIP*-expressing INs were maintained. Of note, meningeal infiltration of plasma cells expressing *IGHG1* and *MZB1* (which predominated over *SKAP1*<sup>+</sup> T cells) was a common finding in sulci with underlying demyelination of the upper cortical layer and loss of *CUX2*-expressing neurons<sup>7,20</sup> (Extended Data Fig. 3b).

We next used smFISH to validate upregulation of cell stress markers, including *PPIA* (encoding prolyl isomerase cyclophilin A, Extended Data Fig. 2a) in MS L2–L3 and L4 ENs. *PPIA* transcripts were increased in neurons from demyelinated and adjacent cortical lesion areas of normal appearance<sup>21</sup> (Fig. 3g). We confirmed upregulation of *NORAD* in L2–L3 and L4 ENs (Extended Data Fig. 2a) by chromogenic and

lesion areas from same sections; representative images). **g**, Upregulation of neuronal *PPIA* in DMGM and NAGM versus control GM (left, white circles indicate perinuclear areas of *PPIA* quantification). Neuronal upregulation and cytoplasmic accumulation of *NORAD* in DMGM versus NAGM and control areas (right, black arrowheads). ANOVA with Tukey's multiple comparison tests was performed (control,  $n = 3$ ; MS,  $n = 4$ ;  $**P \leq 0.01$ ,  $***P \leq 0.001$ ,  $****P \leq 0.0001$ ; different samples with NAWM and DMGM areas from same sections; representative images). Data are mean  $\pm$  s.e.m. For *t*-SNE plots, data are shown from 48,919 nuclei (control,  $n = 9$ ; MS,  $n = 12$ ). Violin plots represent DGE (normalized log-transformed unique molecular identifiers (UMIs)) in L2–L3 EN (L2–L3 EN-A and L2–L3 EN-B) nuclei (control,  $n = 3,481$ ; MS,  $n = 2,639$ ); box plots represent median and standard deviation of gene expression. Scale bars: **b**, **g** (left), 500  $\mu$ m; **d**, 100  $\mu$ m; **e**, 10  $\mu$ m; **f** (top left, top right), 100  $\mu$ m; **f** (bottom right), 20  $\mu$ m; **g** (top right), 20  $\mu$ m; **g** (bottom centre), 5  $\mu$ m.

fluorescent smFISH, and observed cytoplasmic *NORAD* accumulation in MS lesions relative to normal-appearing areas with intact myelin (Fig. 3g). Together, these findings confirm degeneration and selective loss of *CUX2*-expressing upper-layer ENs in cortical MS lesions, whereas co-located inhibitory and other cortical EN subtypes were relatively preserved.

### Distinct spatial macroglial signatures

Previous studies have indicated differential gene expression (DGE) and functionally diverse properties of reactive astrocytes that can be antagonistic or beneficial to repair after injury<sup>22,23</sup>. We identified astro-

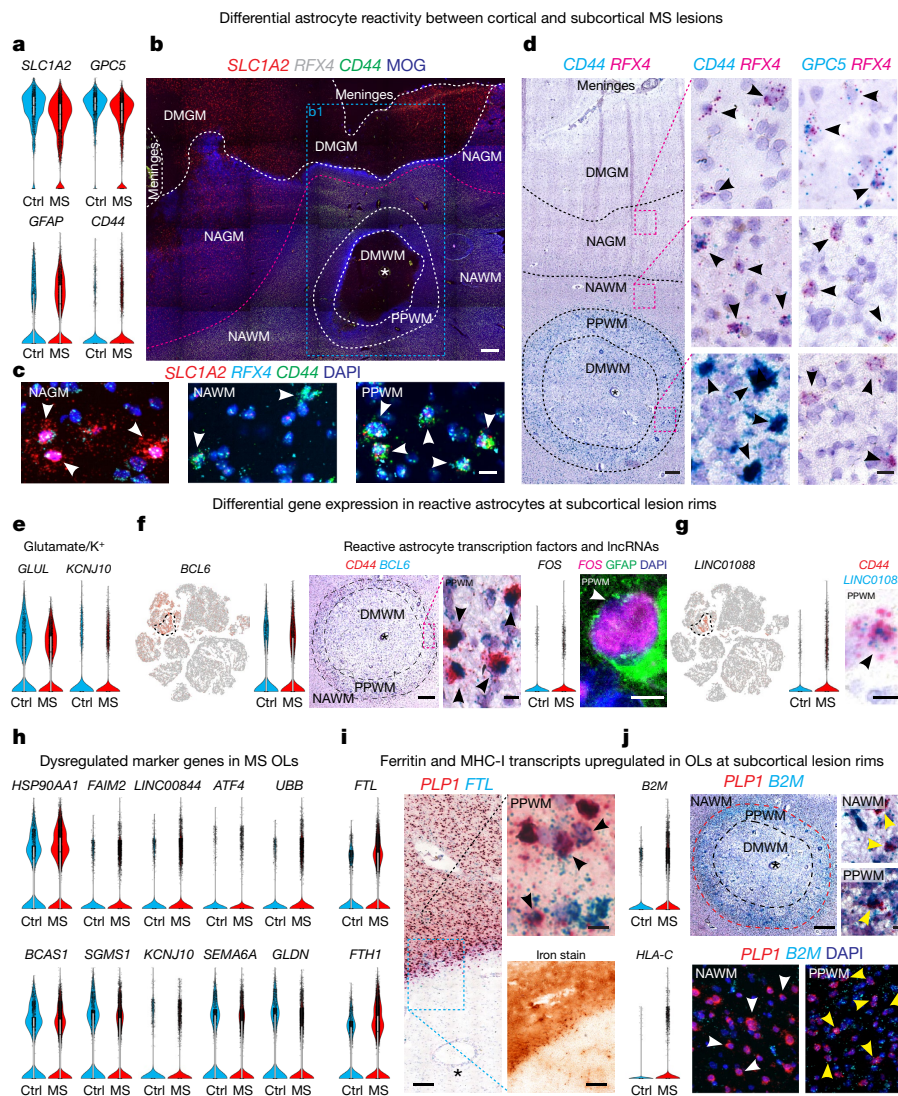


**Fig. 4 | Transcriptomic changes in astrocytes and myelinating OLs in cortical and subcortical MS lesions.** **a**, Downregulation of *SLC1A2* and *GPC5* and upregulation of *GFAP* and *CD44* in MS astrocytes. Ctrl, control. **b**, LAST in situ hybridization experiments confirm *SLC1A2* downregulation in DMGM underlying meningeal inflammation, whereas *CD44* shows ubiquitous expression in NAWM and PPWM (periplaque white matter, centre left) and upregulation in reactive astrocytes at lesion rims in b1 (centre right). The white star indicates a blood vessel. **c, d**, *SLC1A2* (c, white arrowheads), *CD44* (c, white arrowheads) and *GPC5* (d, black arrowheads) co-expression with pan-astrocyte marker *RFX4* and association of *CD44* with fibrous or reactive WM astrocytes (c, d, white and black arrowheads) and *GPC5* (d, black arrowheads) with protoplasmic cortical GM astrocytes. **e**, Downregulation of *GLUL* and *KCNJ10* in MS astrocytes. **f, g**, Differential upregulation of *BCL6* and *FOS* in reactive astrocytes at PPWM (f, black arrowheads) and *LINC01088* in fibrous or reactive WM astrocytes (g, black arrowhead). **h**, Violin

plots for selected genes linked to cell stress (upregulated, top), myelin biosynthesis and axon maintenance (downregulated, bottom) in MS OLs. **i**, *FTL* and *FTH1* upregulation in *PLP1*-expressing OLs at iron-rich lesion rims (left, black arrowheads). **j**, Differential upregulation of *B2M* and *HLA-C* in *PLP1*-expressing OLs at PPWM (right; yellow arrowheads; white arrowheads mark OLs without *B2M* in situ hybridization signals in NAWM). Representative images of in situ hybridization shown (control,  $n = 3$ ; MS,  $n = 4$ ). For *t*-SNE plots, data are shown for a total of 48,919 nuclei (control,  $n = 9$ ; MS,  $n = 12$ ). Violin plots represent DGE (normalized log-transformed UMIs) in nuclei (astrocytes: control,  $n = 1,571$ ; MS,  $n = 3,810$ ; OLs: control,  $n = 3,070$ ; MS,  $n = 9,324$ ); box plots represent median and standard deviation of gene expression. Black asterisks indicate blood vessels. Scale bars: **b, d** (left), **f** (left), **j** (top left), **c, d** (right), **f** (middle), **g, i** (top right), **j** (top right), **f** (right), **5  $\mu\text{m}$ ; **i** (left), **100  $\mu\text{m}$ ; **i** (bottom right), **50  $\mu\text{m}$ ; **j** (bottom right), **20  $\mu\text{m}$ .********

gliosis by enhanced immunoreactivity for glial fibrillary acidic protein (GFAP) in regions of subcortical demyelinated WM that did not cross into the demyelinated cortex in MS lesions (Extended Data Fig. 4a). The GFAP signature in demyelinated WM overlapped with *CD44*-expressing reactive astrocytes<sup>24</sup>; *CD44* was upregulated at the lesion rim in astrocytes that co-expressed *CRYAB* and *MT3*<sup>25</sup> (Extended Data Fig. 4a, b). *RFX4* expression was specific to the astrocyte lineage and captured all *SLC1A2*-expressing GM astrocytes and *CD44*-expressing WM astrocytes (Fig. 4a–d, Extended Data Fig. 4a, Supplementary Table 3). We observed downregulation of regulatory genes encoding proteins that are relevant for glutamate (*SLC1A2* and *GLUL*) and potassium (*KCNJ10*)<sup>26</sup> homeostasis in cortical GM astrocytes and confirmed

expression of *GPC5*, a marker that co-localizes with *RFX4*-expressing GM astrocytes, in lesion and non-lesion cortical areas in situ (Fig. 4a–e, Extended Data Fig. 4a). Reactive astrocytes at inflammatory chronically active lesion rims showed strong expression of the transcription factors *BCL6* and *FOS*, which were associated with upregulation of astrocyte endothelin receptor type B (*EDNRB*), and *LINC01088*<sup>27</sup> (Fig. 4f, g, Extended Data Fig. 4b). Thus, spatial transcriptomics revealed distinct expression patterns for cortical versus subcortical reactive astrocytes in the MS lesion microenvironment.

Myelinating OLs characterized by myelin gene expression and the transcription factor *ST18* (Fig. 1d, Extended Data Fig. 4c) exhibited the third-highest number of differentially expressed genes (Fig. 1g),

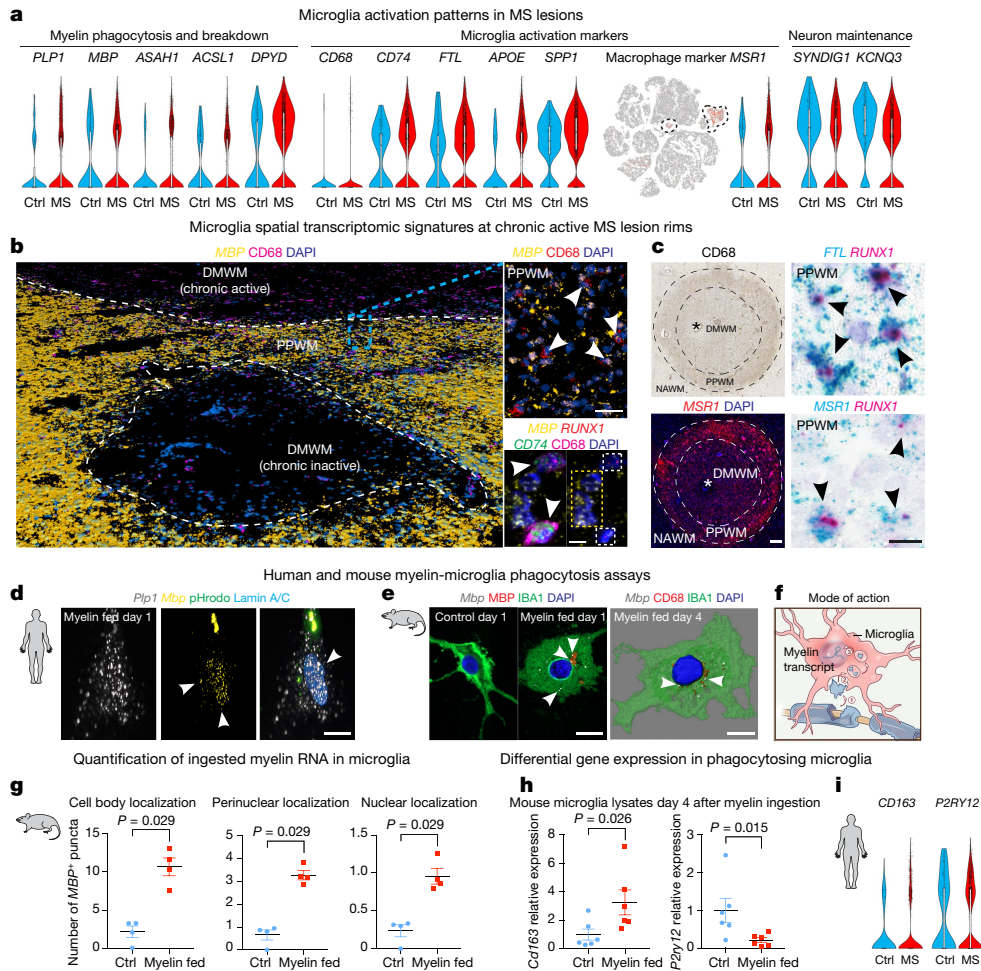


**Fig. 5 | Transcriptomic changes in activated and phagocytosing microglia subsets.** **a**, Violin and *t*-SNE plots for upregulated genes in MS microglia linked to myelin phagocytosis and breakdown (left) and microglia activation and iron handling (middle), and downregulation of genes encoding for synapse function (*SYNDIG1*) and potassium homeostasis (*KCNQ3*) (right). **b**, Left, pseudo low-resolution three-dimensional rendering of stitched 40 $\times$  confocal images showing subcortical WM lesions of different inflammatory stages by *MBP* smFISH and *CD68* immunohistochemistry. Top right, expanded view of the area bound in blue. White arrowheads indicate *CD68*<sup>+</sup> cells with *MBP*<sup>+</sup> in situ hybridization signals. Bottom right, colocalization of *MBP*, *CD74* and *RUNX1* in *CD68*-positive cells (white arrowheads, outlined in white; *MBP*-expressing OLs outlined in yellow). **c**, Immunohistochemistry for *CD68* identifies a WM lesion (top left; black star, blood vessel) with upregulation of *MSR1* at lesion rims (bottom left). In PPWM region, *MSR1* is co-expressed with *RUNX1* (bottom right, arrowheads) and *FTL* (top right, arrowheads). Representative images from different tissue sections (control,  $n = 3$ ; MS,  $n = 4$ ). **d**, **e**, Human (**d**;  $n = 3$  individual biopsies;

consistent with the enriched stress pathways (Extended Data Fig. 4d) and known cell loss in MS. DGE analysis indicated upregulation of genes associated with the heat-shock response (*HSP90AA1*) (Extended Data Fig. 4e), cell stress (*FAIM2* and *ATF4*), iron accumulation (*FTL* and *FTH1*)<sup>28</sup>, major histocompatibility complex (MHC) class I upregulation (*B2M* and *HLA-C*), ubiquitin-mediated protein degradation (*UBB*) and *NORAD* and *LINC00844* (Fig. 4h–j, Extended Data Fig. 2a). Conversely, we observed downregulation of markers for OL differentiation and myelin synthesis (*BCAS1*, *SGMS1*)<sup>29</sup>, potassium homeostasis (*KCNJ10*)<sup>26</sup>, cell–cell interaction (*SEMA6A*) and formation of the node of Ranvier (*GLDN*) in MS OLs at lesion borders (Fig. 4h). Our findings indicate severe cell stress in MS OLs that can be mapped back to periplaque rim areas of subcortical lesions.

microglia labelled with pHrodo with lamin A/C counterstain) and mouse ( $n = 4$  independent cultures; microglia labelled with antibodies against *IBA1* and *CD68* with *DAPI* counterstain) myelin–microglia engulfment assays confirming ingestion of *Mbp* and *Pip1* transcripts derived from rat myelin. Note localization to nuclear–perinuclear spaces (white arrowheads). **f**, Schematic illustrates myelin phagocytosis and uptake into microglial nuclear and perinuclear spaces. **g**, **h**, Quantification of smFISH, showing *Mbp* persistence up to four days after ingestion in mouse microglia (**g**; 4 independent cultures); note upregulation of *Cd163* and downregulation of *P2ry12* in phagocytosing mouse microglia (**h**; 6 independent cultures). **i**, Upregulation of *CD163* and downregulation of *P2RY12* in human MS microglia. Two-tailed Mann–Whitney *U*-tests. Data are mean  $\pm$  s.e.m. For *t*-SNE plots, data are from a total of 48,919 nuclei (control,  $n = 9$ ; MS,  $n = 12$ ). Violin plots represent DGE (normalized log transformed UMIs) in microglia nuclei (control,  $n = 159$ ; MS,  $n = 1,524$  (microglial and phagocytosing cells)); box plots represent median and standard deviation of gene expression. Scale bars: **b** (top right), 50  $\mu$ m; **b** (bottom right), **e**, 10  $\mu$ m; **c** (left), 200  $\mu$ m; **c** (right), **d**, 20  $\mu$ m.

### Activated phagocytosing cells in MS

On the basis of the marked expansion of microglia in MS samples (Fig. 1e), we performed hierarchical clustering (Extended Data Fig. 5) and observed microglial cells with a homeostatic gene expression signature (*P2RY12*, *RUNX1* and *CSF1R*) in MS and control samples as well as MS-specific cells with enrichment for transcripts encoding activation markers, complement factors, MHC class II-associated proteins<sup>14</sup> and lipid degradation proteins (*ASAHI*, *ACSL1*, *DPYD*) (Fig. 5a–c, Extended Data Fig. 5, Supplementary Table 5). Downregulated genes in MS microglia included synapse-remodelling transcript *SYNDIG1* and potassium channel *KCNQ3*. Marker genes for microglia reactivity (*CD68*, *CD74*, *FTL* and *MSR1*) co-localized with the lineage microglia marker *RUNX1*, and mapped such activated cells to chronic active boundaries of subcortical MS lesions (Fig. 5a–c).

Of note, we identified a cluster of microglial cells characterized by phagocytosis and enrichment for OL-specific markers *PLP1*, *MBP* and *ST18* (Fig. 1c, d, Extended Data Figs. 4c, 5, Supplementary Table 7), suggesting the possibility that ingested myelin transcripts co-purified with nuclei of phagocytosing cells in MS. To provide functional evidence for putative myelin RNA microglial phagocytosis, we cultured human and mouse microglia exposed to purified myelin from rat brain (Fig. 5d–i), which contains myelin transcripts<sup>30</sup> (Extended Data Fig. 6). *Plp1* and *Mbp* transcripts were observed in intracellular, perinuclear and nuclear compartments of cultured human or mouse microglia one day after exposure to pHrodo-labelled myelin, and ingested *Mbp* mRNA was observed in mouse microglia up to four days after feeding. In parallel, we observed morphological changes in phagocytosing mouse microglia, differential upregulation of the activation marker *Cd163* and downregulation of the homeostatic microglia marker *P2ry12*<sup>31</sup> (Fig. 5d–i). These changes in mouse microglia were reflected in gene expression changes in human MS microglia detected by snRNA-seq (Fig. 5i). We have created an interactive web browser to analyse cell-type specific expression levels of genes and transcriptomic changes in MS versus control tissue (<https://ms.cells.ucsc.edu>).

## Discussion

MS lesions are heterogeneous in cortical and subcortical areas, and have distinct patterns of inflammatory demyelination<sup>10,32,33</sup>. We found cell-type-specific changes in gene expression in regions of cortical neurodegeneration and at the rim of chronic active subcortical lesions involved in progression and cortical atrophy. Our technical finding of the feasibility of snRNA-seq in MS tissue is consistent with recent observations<sup>13–15</sup>. We used high-quality archival samples from patients, who did not receive modern immunomodulatory therapies; thus, they represent the end point of the natural disease course with relatively early death of patients (30–50 years of age). However, the number of MS samples studied could have resulted in under-reporting of certain lineages.

Computational analysis of DGE and trajectory analysis of a total of 12 MS and 9 control samples pointed most strongly to the neuronal compartment and indicated substantial cellular stress and loss of *CUX2*-expressing upper-layer ENs in demyelinated and partially remyelinated cortical MS lesions. As such lesions underlie meningeal inflammation with pronounced plasma B cell infiltration, these findings highlight the importance of B cells in progressive MS<sup>7,8</sup> and that damaged cortical neuron populations may potentially benefit from B-cell-depleting therapies<sup>34</sup>.

We validated candidate gene expression using spatial transcriptomics of human MS brain samples. Markers of stressed *CUX2*-expressing neurons included *PPIA* (which encodes cyclophilin A) and *NORAD*, a neuronal lncRNA that helps to stabilize DNA following genomic stress by binding to pumilio and RBMX proteins<sup>17,35</sup>, as well as other pathways for protein degradation, heat-shock response and metabolic exhaustion<sup>36,37</sup>. Whereas most transcriptional changes and neuronal cell loss occurred in demyelinated regions, we also observed abnormal gene expression (for example, *PPIA*) in cortical areas with normal appearance, suggesting a gradient of pathology<sup>38</sup>. While it is possible that in MS, *CUX2*-expressing projection neurons are damaged by both sustained meningeal inflammation and retrograde axon pathology from juxtacortical WM lesions<sup>33</sup>, additional intrinsic factors might account for their lack of resilience, especially considering that neighbouring inhibitory and ENs of the cortex exhibited relatively little cell loss.

Recent studies have used MS WM lesion snRNA-seq and single-cell RNA-seq to study the OL<sup>13</sup> and microglia<sup>14</sup> lineages and reported subsets linked to MS pathobiology. Here, we used spatial transcriptomics to map dysregulated glial gene expression in cortical and subcortical lesion and non-lesion areas. Transcriptomic changes associated with OL, microglia and astrocyte activation mapped predominantly to the rim areas of chronically active subcortical lesions<sup>11,39</sup>. In particular, lesion rim OLs<sup>28</sup> showed molecular changes indicating cellular

degeneration and iron overload. Notably, stressed myelinating OLs and upper-layer cortical projection neurons both upregulated genes for self-antigen presentation to immune cells (*B2M* and *HLA-C*), indicating processes that perpetuate degeneration and inflammation<sup>40,41</sup>.

In another example of spatial diversity in MS, we detected distinct transcripts for cortical astrocytes versus subcortical lesion astrocytes, indicating molecular differences in the tissue microenvironment. Furthermore, we found that snRNA-seq can distinguish phagocytosing cells in MS on the basis of their transport of ingested myelin transcripts into perinuclear structures or the nucleus itself. Future work is needed to determine whether this biology is beneficial or detrimental in disease course, for example, by exacerbating inflammation. In summary, multilineage and spatial gene expression analysis indicates cell-type-specific neuron vulnerability and glial activation patterns relevant to neurodegeneration and MS lesion progression.

## Online content

Any methods, additional references, Nature Research reporting summaries, source data, extended data, supplementary information, acknowledgements, peer review information; details of author contributions and competing interests; and statements of data and code availability are available at <https://doi.org/10.1038/s41586-019-1404-z>.

Received: 26 October 2018; Accepted: 12 June 2019;

Published online: 17 July 2019

1. GBD 2015 Disease and Injury Incidence and Prevalence Collaborators. Global, regional, and national incidence, prevalence, and years lived with disability for 310 diseases and injuries, 1990–2015: a systematic analysis for the Global Burden of Disease Study 2015. *Lancet* **388**, 1545–1602 (2016).
2. Reich, D. S., Lucchinetti, C. F. & Calabresi, P. A. Multiple sclerosis. *N. Engl. J. Med.* **378**, 169–180 (2018).
3. Lassmann, H. Multiple sclerosis pathology. *Cold Spring Harb. Perspect. Med.* **8**, a028936 (2018).
4. Trapp, B. D. et al. Axonal transection in the lesions of multiple sclerosis. *N. Engl. J. Med.* **338**, 278–285 (1998).
5. Schirmer, L., Antel, J. P., Brück, W. & Stadelmann, C. Axonal loss and neurofilament phosphorylation changes accompany lesion development and clinical progression in multiple sclerosis. *Brain Pathol.* **21**, 428–440 (2011).
6. Peterson, J. W., Bö, L., Mörk, S., Chang, A. & Trapp, B. D. Transected neurites, apoptotic neurons, and reduced inflammation in cortical multiple sclerosis lesions. *Ann. Neurol.* **50**, 389–400 (2001).
7. Magliozzi, R. et al. Meningeal B-cell follicles in secondary progressive multiple sclerosis associate with early onset of disease and severe cortical pathology. *Brain* **130**, 1089–1104 (2007).
8. Magliozzi, R. et al. A gradient of neuronal loss and meningeal inflammation in multiple sclerosis. *Ann. Neurol.* **68**, 477–493 (2010).
9. Lucchinetti, C. F. et al. Inflammatory cortical demyelination in early multiple sclerosis. *N. Engl. J. Med.* **365**, 2188–2197 (2011).
10. Trapp, B. D. et al. Cortical neuronal densities and cerebral white matter demyelination in multiple sclerosis: a retrospective study. *Lancet Neurol.* **17**, 870–884 (2018).
11. Dal-Bianco, A. et al. Slow expansion of multiple sclerosis iron rim lesions: pathology and 7 T magnetic resonance imaging. *Acta Neuropathol.* **133**, 25–42 (2017).
12. Mainero, C. et al. A gradient in cortical pathology in multiple sclerosis by in vivo quantitative 7 T imaging. *Brain* **138**, 932–945 (2015).
13. Jäkel, S. et al. Altered human oligodendrocyte heterogeneity in multiple sclerosis. *Nature* **566**, 543–547 (2019).
14. Masuda, T. et al. Spatial and temporal heterogeneity of mouse and human microglia at single-cell resolution. *Nature* **566**, 388–392 (2019).
15. Lake, B. B. et al. Neuronal subtypes and diversity revealed by single-nucleus RNA sequencing of the human brain. *Science* **352**, 1586–1590 (2016).
16. Lodato, S. & Arlotta, P. Generating neuronal diversity in the mammalian cerebral cortex. *Annu. Rev. Cell Dev. Biol.* **31**, 699–720 (2015).
17. Lee, S. et al. Noncoding RNA *NORAD* regulates genomic stability by sequestering PUMILIO proteins. *Cell* **164**, 69–80 (2016).
18. Mus, E., Hof, P. R. & Tiedge, H. Dendritic BC200 RNA in aging and in Alzheimer's disease. *Proc. Natl Acad. Sci. USA* **104**, 10679–10684 (2007).
19. Bayraktar, O. A. et al. Single-cell in situ transcriptomic map of astrocyte cortical layer diversity. Preprint at <https://doi.org/10.1101/432104> (2018).
20. Machado-Santos, J. et al. The compartmentalized inflammatory response in the multiple sclerosis brain is composed of tissue-resident CD8<sup>+</sup> T lymphocytes and B cells. *Brain* **141**, 2066–2082 (2018).
21. Pasetto, L. et al. Targeting extracellular cyclophilin A reduces neuroinflammation and extends survival in a mouse model of amyotrophic lateral sclerosis. *J. Neurosci.* **37**, 1413–1427 (2017).

22. Liddel, S. A. et al. Neurotoxic reactive astrocytes are induced by activated microglia. *Nature* **541**, 481–487 (2017).
23. Anderson, M. A. et al. Astrocyte scar formation aids central nervous system axon regeneration. *Nature* **532**, 195–200 (2016).
24. Chang, A. et al. Cortical remyelination: a new target for repair therapies in multiple sclerosis. *Ann. Neurol.* **72**, 918–926 (2012).
25. Ousman, S. S. et al. Protective and therapeutic role for  $\alpha$ B-crystallin in autoimmune demyelination. *Nature* **448**, 474–479 (2007).
26. Schirmer, L. et al. Differential loss of KIR4.1 immunoreactivity in multiple sclerosis lesions. *Ann. Neurol.* **75**, 810–828 (2014).
27. Gadea, A., Schinelli, S. & Gallo, V. Endothelin-1 regulates astrocyte proliferation and reactive gliosis via a JNK/c-Jun signaling pathway. *J. Neurosci.* **28**, 2394–2408 (2008).
28. Hametner, S. et al. Iron and neurodegeneration in the multiple sclerosis brain. *Ann. Neurol.* **74**, 848–861 (2013).
29. Fard, M. K. et al. BCAS1 expression defines a population of early myelinating oligodendrocytes in multiple sclerosis lesions. *Sci. Transl. Med.* **9**, eaam7816 (2017).
30. Brophy, P. J., Boccaccio, G. L. & Colman, D. R. The distribution of myelin basic protein mRNAs within myelinating oligodendrocytes. *Trends Neurosci.* **16**, 515–521 (1993).
31. Zrzavy, T. et al. Loss of ‘homeostatic’ microglia and patterns of their activation in active multiple sclerosis. *Brain* **140**, 1900–1913 (2017).
32. Lucchinetti, C. et al. Heterogeneity of multiple sclerosis lesions: implications for the pathogenesis of demyelination. *Ann. Neurol.* **47**, 707–717 (2000).
33. Haider, L. et al. The topography of demyelination and neurodegeneration in the multiple sclerosis brain. *Brain* **139**, 807–815 (2016).
34. Hauser, S. L. et al. B-cell depletion with rituximab in relapsing-remitting multiple sclerosis. *N. Engl. J. Med.* **358**, 676–688 (2018).
35. Munschauer, M. et al. The *NORAD* lncRNA assembles a topoisomerase complex critical for genome stability. *Nature* **561**, 132–136 (2018).
36. Campbell, G. R. et al. Mitochondrial DNA deletions and neurodegeneration in multiple sclerosis. *Ann. Neurol.* **69**, 481–492 (2011).
37. Fischer, M. T. et al. Disease-specific molecular events in cortical multiple sclerosis lesions. *Brain* **136**, 1799–1815 (2013).
38. Carassiti, D. et al. Neuronal loss, demyelination and volume change in the multiple sclerosis neocortex. *Neuropathol. Appl. Neurobiol.* **44**, 377–390 (2018).
39. Absinta, M. et al. Persistent 7-tesla phase rim predicts poor outcome in new multiple sclerosis patient lesions. *J. Clin. Invest.* **126**, 2597–2609 (2016).
40. Falcão, A. M. et al. Disease-specific oligodendrocyte lineage cells arise in multiple sclerosis. *Nat. Med.* **24**, 1837–1844 (2018).
41. Kirby, L. et al. Oligodendrocyte precursor cells are co-opted by the immune system to cross-present antigen and mediate cytotoxicity. Preprint at <https://doi.org/10.1101/461434> (2018).

**Publisher’s note:** Springer Nature remains neutral with regard to jurisdictional claims in published maps and institutional affiliations.

© The Author(s), under exclusive licence to Springer Nature Limited 2019

## METHODS

No statistical methods were used to predetermine sample size. The experiments were not randomized. The investigators were not blinded to allocation during experiments and outcome assessment.

**Human tissue samples, ethical compliance and clinical information.** All tissue included in this study was provided by the UK Multiple Sclerosis Tissue Bank at Imperial College, London and the University of Maryland Brain Bank through the NIH NeuroBioBank. Human MS and control tissues were obtained via a prospective donor scheme following ethical approval by the National Research Ethics Committee in the UK (08/MRE09/31). We have complied with all relevant ethical regulations regarding the use of human postmortem tissue samples. We examined a total of 35 (19 MS and 16 controls) snap-frozen brain tissue blocks obtained at autopsies from 17 MS patients and 16 controls.

**RNA extraction and integrity measurements.** Frozen brain tissue samples encompassing the entire span of cortical GM with attached meninges and underlying subcortical WM were sectioned on a CM3050S cryostat (Leica Microsystems) to collect 100- $\mu$ m-thick sections for total RNA and nucleus isolation. Total RNA from 10 mg tissue was isolated using TRIzol (Thermo Fisher) and purified using the RNeasy Kit (Qiagen) according to the manufacturer's instructions. Next, we performed RNA integrity analysis on the Agilent 2100 Bioanalyzer using the RNA 6000 Pico Kit (Agilent). Only samples with an RNA integrity number (RIN)  $\geq 6.5$  were used to perform the isolation of nuclei followed by snRNA-seq as samples with lower RIN generated low-quality data. As the result, we excluded 14 samples (7 MS and 7 control samples) and performed snRNA-seq on a total of 12 snap-frozen brain tissue blocks obtained at autopsies from 7 female and 3 male patients with MS (1 primary progressive MS, 9 secondary progressive MS; Supplementary Table 1). The age of the MS patients ranged from 34 to 55 years (median 46 years), and the disease duration from 5 to 43 years (median 18 years). For control tissue, we included a total of nine snap-frozen brain tissue blocks obtained at autopsies from four female and five male individuals. The age of control patients ranged from 35 to 82 years (median 54 years; Supplementary Table 1).

**Isolation of nuclei and snRNA-seq on the 10x Genomics platform.** Control and MS samples were processed in the same nucleus isolation batch to minimize potential batch effects. In brief, 40 mg of sectioned brain tissue was homogenized in 5 ml of RNase-free lysis buffer (0.32 M sucrose, 5 mM  $\text{CaCl}_2$ , 3 mM  $\text{MgAc}_2$ , 0.1 mM EDTA, 10 mM Tris-HCl pH 8, 1 mM DTT, 0.1% Triton X-100 in DEPC-treated water) using a glass Dounce homogenizer (Thomas Scientific) on ice<sup>42</sup>. The homogenate was loaded into a 30-ml thick-polycarbonate ultracentrifuge tube (Beckman Coulter). Then, 9 ml of sucrose solution (1.8 M sucrose, 3 mM  $\text{MgAc}_2$ , 1 mM DTT, 10 mM Tris-HCl in DEPC-treated water) was added to the bottom of the tube under the homogenate and centrifuged at 107,000g for 2.5 h at 4°C. Supernatant was aspirated, and nuclear pellet was incubated in 250  $\mu$ l of DEPC-treated water-based PBS for 20 min on ice before resuspending the pellet. Suspensions of nuclei were analysed for the presence of debris, nuclei were counted using a haemocytometer and diluted to 2,000 nuclei per  $\mu$ l before performing single-nucleus capture using the 10x Genomics Single-Cell 3' system (Extended Data Fig. 1a). Target capture of 4,000 nuclei per sample was used. Control and MS samples were loaded on the same 10x chip to minimize potential batch effects. Single-nucleus libraries from individual samples were pulled and sequenced on the Illumina HiSeq 2500 machine. The 10x nucleus capture and library preparation protocol was carried out according to the manufacturer's recommendation without modification.

**snRNA-seq data processing with 10x Genomics Cell Ranger software and data filtering.** For library demultiplexing, fastq file generation, read alignment and unique molecular identifier (UMI) quantification, Illumina bcl2fastq v.2.19 and Cell Ranger software v.1.3.1 were used. Cell Ranger was used with default parameters, except for using a pre-mRNA reference file (ENSEMBL GRCh38) to ensure capturing intronic reads originating from pre-mRNA transcripts abundant in the nuclear fraction.

Individual expression matrices containing numbers of UMIs per gene in each nucleus were filtered to retain nuclei with at least 500 genes and 1,000 transcripts expressed. Genes expressed in less than three nuclei were filtered out. Mitochondrial RNA genes were filtered out as well to exclude transcripts originating from outside the nucleus and avoid biases introduced by the isolation of nuclei and ultracentrifugation. Individual matrices were combined, UMIs were normalized to the total UMIs per nucleus and log-transformed.

**Dimensionality reduction, clustering and *t*-SNE visualization.** A filtered log-transformed UMI matrix containing genes expressed in more than five cells was used to perform truncated singular value decomposition with  $k = 50$  using the svd R software package from base package v.3.6.0. A screen plot was generated to select the numbers of significant principle components (PCs) by localizing the last PC before the explained variance reaches plateau. This resulted in selection of 11 PCs. The significant PCs were used to calculate Jaccard distance-weighted nearest neighbour distances; the number of nearest neighbours was assigned to root

square of number of nuclei. The resulting graph with Jaccard-weighted edges was used to perform Louvain clustering using the igraph R software package v.1.0.1<sup>43</sup>. To visualize the transcriptomic profiles of nuclei in two-dimensional space, *t*-SNE was performed using the Python software module MulticoreTSNE v.1.0.0<sup>44</sup>. Several original clusters expressed a combination of cell type markers, including IN subtypes, T cells, B cells, stromal cells and endothelial cells. These clusters were further subclustered by repeating principal component analysis of selected cell populations and performing partitioning around medoids bi-clustering (Supplementary Table 2).

**Cell-type annotation.** Cell types were annotated based on the expression of known marker genes visualized by *t*-SNE plot, as well as by performing unbiased gene marker analysis (Supplementary Table 3). For the latter, the Model-based Analysis of Single-cell Transcriptomics (MAST) R package v.1.10.0<sup>45</sup> was used to perform DGE analysis by comparing nuclei in each cluster to the rest of nuclear profiles. Genes with a FDR-adjusted  $P < 0.05$  and at least twofold gene expression upregulation were selected as cell type markers. Subtypes of projection neurons and INs were annotated based on combinatorial expression of inhibitory and excitatory markers and projection neurons and IN subtype markers.

**Quantification of number of cell for cell types in MS and control samples.** To get insight into enrichment or depletion of cell types in MS, numbers of nuclei in each cluster and individuals were normalized to the total number of nuclei captured from each individual. The following formulae were used:

$$\text{Normalization factor} = \frac{\text{Total nuclei in sample}}{\text{Total nuclei in sample with largest number of total nuclei captured}}$$

$$\text{Normalized cell number} = \frac{\text{Raw cell number in a cell type captured from a sample}}{\text{Normalization factor}}$$

Then, normalized cell numbers in each sample and cell type were compared between MS and control groups using a Mann–Whitney *U*-test (Supplementary Table 4).

**DGE analysis based on repeated down sampling.** To estimate the degree to which the disease affects different cell types of the central nervous system, the number of differentially expressed genes between patients with MS and controls was used as a surrogate parameter. We reasoned that the power to identify differentially expressed genes is partially dependent on the number of cells detected in each cluster. Thus, we devised an analytical approach that corrects for cell count based on repeated downsampling to identical cell numbers for each donor–cluster combination. Specifically, 100 iterations of downsampling were performed, for which 20 cells were randomly drawn from each donor for each cluster and combined into synthetic bulk samples as input for a DGE analysis using DESeq2 v.1.20.0<sup>46</sup>. In this case, we favoured a computationally less intensive analysis using DESeq2 without covariates on synthetic bulk samples over MAST to facilitate the execution of a sufficient number of iterations. The results of this screening approach were plotted as notched box plots and relevant differences between clusters were assumed in cases in which notches did not overlap (Fig. 1g). Notably, very small clusters that had fewer than 4 samples with a minimum of 20 cells available were excluded from the analysis.

**Trajectory pseudotime analysis.** A single-cell trajectory for excitatory cortical layer 2 and 3 (*CUX2*-expressing) neurons was determined and analysed using the Monocle package v.3 alpha<sup>47</sup>. FDR-corrected  $P$  values were calculated using the Monocle 3alpha R package using 5,938 L2–L3 EN nuclei (Supplementary Table 5). In brief, single-cell transcriptomes of all *CUX2*-expressing cells were dimensionally reduced by principal component analysis followed by uniform manifold approximation and projection. Next, an unsupervised trajectory through the reduced space was identified using the SimplePPT algorithm. The root of the resulting tree was set to where most cells of the control samples clustered. Pseudotime values were then automatically assigned to each cell depending on its distance on the trajectory relative to the root node. Moran's *I* test as implemented in Monocle 3 alpha was used to identify genes significantly regulated over pseudotime. For each gene, the adjusted  $P$  value was signed according to the direction of regulation determined by comparing expression in the first 5% of cells in pseudotime with the last 5%. The resulting gene list, ordered by sign-adjusted  $P$  value, was the input for gene set enrichment analysis to test for enriched gene ontology (GO) terms using the clusterProfiler package v.3.10.1<sup>48</sup>. Gene sets with a FDR-corrected  $P < 0.05$  were considered to be significantly enriched. The results of the analysis were plotted as a GO term map using the `emaplot()` function of the clusterProfiler package to cluster terms based on their gene set relation. Clusters of gene sets were annotated with representative labels.

To analyse enrichment of individual gene sets on a single-cell level, we used the AUCell algorithm<sup>49</sup>. The algorithm measures gene-set enrichment towards the top of an expression-ranked gene list for each cell. The resulting area under the curve values (AUC) were plotted for all cells along pseudotime.

**DGE analysis using linear mixed-model regression.** To identify genes differentially expressed in MS compared to control samples per cell type, *P* values were calculated and FDR-corrected using MAST. All nuclei from 9 control and 12 MS samples for corresponding cell types were used (Supplementary Table 6). MAST was used to perform zero-inflated regression analysis by fitting a linear mixed model. To exclude gene expression changes stemming from confounders, such as age, sex, RIN, cortical region, fractions of ribosomal and mitochondrial transcripts, 10x capture batch and sequencing batch, the following model was fit with MAST:

$$\begin{aligned} \text{zlm}(\sim & \text{diagnosis} + \text{sequencer} + (1|\text{ind}) + \text{cngeneson} + \text{age} + \text{sex} + \text{RIN} \\ & + \text{region} + \text{Capbatch} + \text{Seqbatch} + \text{ribo}_{\text{perc}} + \text{mito}_{\text{perc}} \text{ sca, method} \\ = & \text{glmer, ebayes} = \text{F, silent} = \text{T}) \end{aligned}$$

Where *cngeneson* is gene detection rate (factor recommended in MAST tutorial), *Capbatch* is 10x capture batch, *Seqbatch* is sequencing batch, *ind* is individual label, *ribo\_perc* is ribosomal RNA fraction and *mito\_perc* is mitochondrial RNA fraction.

To identify genes differentially expressed due to the disease effect, likelihood ratio test was performed by comparing the model with and without the diagnosis factor. Genes with at least 10% increase or decrease in expression in MS versus control and an FDR-corrected  $P < 0.05$  were selected as differentially expressed. In addition, we calculated raw fold changes of gene expression by repeating MAST analysis with only the diagnosis factor in the model and filtered out genes with raw fold change of expression less than 7%. The latter filtering step enabled the removal of genes, for which the fold change of expression was heavily dependent on confounding factors, rather than clinical diagnosis.

**GO analysis for differentially expressed genes.** Panther software v.14.0 (<http://geneontology.org>, <http://pantherdb.org>) was used to perform statistical over-representation tests for differentially expressed genes with respect to individual clusters. All genes expressed in a given cluster were used as a background list, and GO-term analysis for enriched biological processes was performed. Processes with an FDR-corrected  $P < 0.05$  were considered and sorted by FDR.

**Heat map data presentation and hierarchical cluster analysis.** Hierarchical clustering was performed with the online Morpheus software (Broad Institute, <https://software.broadinstitute.org/morpheus>) using 1 – Pearson correlation as distance metric and complete clustering of rows (genes) and columns (cells or samples). To perform hierarchical clustering, we used single-nucleus gene expression matrices of cell type markers for lymphocytes, microglia and phagocytes (Extended Data Fig. 3, 5, Supplementary Table 7).

**Immunohistochemistry.** In brief, 16- $\mu\text{m}$ -thick cryosections were collected on superfrost slides (VWR) using a CM3050S cryostat (Leica Microsystems) and fixed in either 4% PFA at room temperature or ice-cold methanol. Next, sections were blocked in 0.1 M PBS, 0.1% Triton X-100, 10% goat, horse or donkey serum for 1 h at room temperature. Primary antibody incubations were carried out overnight at 4°C. The following antibodies were used for immunohistochemistry: mouse anti-MOG (clone 8-18C5, 1:1,000 (1:200 after in situ hybridization), Millipore Sigma), rat anti-GFAP (clone 2.2B10, Thermo Fisher, 1:1,000 (1:200 after in situ hybridization)), rat anti-CD3 (clone CD3-12, Bio-Rad, 1:100), rabbit anti-MZB1 (polyclonal, Thermo Fisher, 1:1,000), rabbit anti-SKAP1 (polyclonal, Sigma-Aldrich, 1:100), mouse anti-CD138 (clone DL-101, Biologend, 1:100), mouse anti-CD68 (clone 514H12, Bio-Rad, 1:100), mouse anti-NeuN (clone MAB377, Millipore Sigma, 1:1,000). After washing in 0.1 M PBS, cryosections were incubated with secondary antibodies diluted in 0.1 M PBS, 0.1% Triton X-100 for 2 h at room temperature. For chromogenic assays, sections were incubated with biotinylated secondary IgG antibodies (1:500, Thermo Fisher) followed by avidin–biotin complex for 1 h incubation (1:500, Vector Labs) and subsequent colour revelation using 3'-diaminobenzidine (DAB) according to the manufacturer's recommendations (DAKO). For immunofluorescence, Alexa fluochrome-tagged secondary IgG antibodies (1:500, Thermo Fisher) were used for primary antibody detection. Slides with fluorescent antibodies were mounted with DAPI Fluoromount-G (Southern Biotech). Negative control sections without primary antibodies were processed in parallel. For diagnostic purposes, haematoxylin and eosin and Luxol fast blue stainings were carried out.

**Iron staining.** Tissue non-haem iron was stained according to previously published protocols<sup>50</sup>. Sections of fixed, frozen human tissue were allowed to warm to room temperature and dried for 15 min in a laminar-flow hood. Endogenous peroxidase activity was quenched by immersion in a solution of 0.3% H<sub>2</sub>O<sub>2</sub> (v/v) in methanol for 20 min and washed three times in deionized water (dH<sub>2</sub>O). Sections were then placed in a solution of fresh 1% (w/v) potassium ferrocyanide (Sigma-Aldrich),

pH 1 with HCl for 40 min, followed by three washes in dH<sub>2</sub>O. Sections were then placed in 0.01M NaN<sub>3</sub>, 0.3% H<sub>2</sub>O<sub>2</sub> in methanol for 60 min, followed by three washes in PBS. Iron staining was intensified using DAB (10% v/v) solution from Pierce DAB substrate kit (Thermo Fisher) in PBS with 0.005% H<sub>2</sub>O<sub>2</sub> (v/v) for 5 h. DAB reaction was halted with three washes in PBS, one wash in 100% methanol and a further three washes in Bond Wash solution (Leica Biosystems).

**Chromogenic single or duplex in situ RNA hybridization.** Single molecule in situ hybridization was performed according to the manufacturer's recommendations (RNAscope 2.5 brown, red and duplex chromogenic manual assay kits, Advanced Cell Diagnostics, Biotechne). Sequences of target probes, preamplifier, amplifier, and label probes are proprietary and commercially available (Biotechne). Typically, target probes contain 20 ZZ probe pairs (approximately 50 bp per pair) covering 1,000 bp. The following human manual RNAscope assay probes were used: *CUX2*, *RORB*, *TLE4*, *THY1*, *VIP*, *SST*, *HSP90AA1*, *LINC00657*, *PPIA*, *FTL*, *B2M*, *PIEZO2*, *IGHG1*, *MSR1*, *LINC01088*, *GPC5*, *CD44*, *BCL6*, *FOS*, *EDNRB*, *ST18*, *RUNX1-C2*, *SLCIA2-C2*, *CD44-C2*, *RFX4-C2*, *PDGFRA-C2*, *SYT1-C2* and *PLP1-C2*. Following red chromogenic smFISH, we performed immunohistochemistry using either chromogenic or fluorescence assays (see above). After duplex single molecule in situ hybridization we performed haematoxylin staining of nuclei.

**Fluorescence multiplex in situ RNA hybridization and human brain tissue optimization.** For smFISH on human brain cryosections performed on an automated BOND RX robotic stainer (Leica), the following procedure was used. Fresh snap-frozen human brain tissue was cryosectioned and slides immediately stored at –80°C. Because human brain tissue often showed high levels of autofluorescence, several treatments were needed to minimize interference with FISH signals. Using spectral analysis, we identified sources of autofluorescence to be mainly lipofuscin in grey matter (emission wavelengths ~450–650 nm) and collagen or elastin in white matter (emission wavelengths ~470–520 nm). Initial experiments in fixed tissue also displayed low levels of formaldehyde-induced fluorescence in the green yellow spectra (~420–470 nm); thus, sections of human brain tissue were not formaldehyde-fixed before storage. On the day of the experiment, with minimal exposure to (room temperature) air to keep oxidation of endogenous fluorescent proteins low, slides were directly transferred from –80°C into pre-chilled PFA 4% (methanol-free). Following 45-min incubation sections where immediately submerged in boiling citrate buffer (pH 3.0, Sigma-Aldrich) for 15 min to loosen up the recent crosslinking. Slides where then rinsed twice in PBS and dehydrated. To avoid interference of background fluorescence, experiments were designed so that low-expressing probes were detected using fluorophores with low background, that is, Opal 570, Opal 650. All samples in this study were treated in the same way regardless of disease stage and age. The assay was then performed for 2–3 genes by FISH using the RNAscope LS Multiplex Assay (Biotechne).

Samples were initially permeabilized with heat and protease treatment to improve probe penetration and hybridization. For heat treatment, samples were incubated in BOND ER2 buffer (pH 9.0, Leica) at 95°C for 10 min. For protease treatment, samples were incubated in ACD protease reagent at 42°C for 10 min. Before probe hybridization, samples were incubated in hydrogen peroxide for 10 min to inactivate endogenous peroxidases and ACD protease. Subsequently, samples were incubated in target  $\alpha$ -probe mixtures (C1–C4) for 2 h at 42°C. Each slide wash flushed three times in order to obtain optimal hybridization to transcripts. The following human RNAscope LS assay probes were used: *SYT1*, *CUX2*, *LINC00657*, *B2M*, *CD74*, *RUNX1*, *RFX4*, *SLCIA2*, *CD44*, *PLP1* and *MBP*.

Following hybridization, branched DNA amplification trees were built through sequential incubations in AMP1, AMP2 and AMP3 reagents for 15–30 min each at 42°C with LS Rinse buffer (Leica) high-stringency washes between incubation steps. After amplification, probe channels were detected sequentially via HRP–TSA labelling. Here, samples were incubated in channel-specific HRP reagents for 15 min at 42°C, TSA fluorophores for 30 min and HRP blocking reagent for 15 min at 42°C. Probes were labelled using Opal 520, 570 and 650 TSA fluorophores (Perkin Elmer, 1:300). Directly following FISH assay, localization of MOG myelin protein was performed by BOND RX assisted immunohistochemistry, where samples were incubated with anti-MOG antibody (clone 8-18C5, Millipore Sigma) in blocking solution for 1 h (1:200). To develop the antibody signal, samples were incubated in donkey anti-mouse HRP (Abcam, 1:500) for 1 h, TSA–biotin (Perkin Elmer, 1:200) for 10 min and streptavidin-conjugated Alexa 700 (Sigma-Aldrich, 1:200) for 30 min.

**PCR for myelin and neuron transcripts from rat myelin preparations.** RNA from myelin was purified using phenol–chloroform extraction by adding 100  $\mu\text{l}$  of chloroform (Sigma-Aldrich) to 500  $\mu\text{l}$  of Tri-Reagent containing 50  $\mu\text{l}$  of enriched rat myelin derived from the central nervous system. Samples were vortexed and centrifuged at 12,000g<sub>max</sub> for 15 min at 4°C. The upper aqueous phase was collected and an equal volume of 70% ethanol added and vortexed. RNA was purified using PureLink RNA Mini-Kit (Thermo Fisher) according to the manufacturer's instructions. RNA was eluted with 30  $\mu\text{l}$  of RNase free water and concentration determined using a SPECTROStar Nano. cDNA was synthesized from 0.3  $\mu\text{g}$  of RNA

using SuperScript III (Thermo Fisher) according to the manufacturer's instructions with or without inclusion of RT enzyme. PCRs for rat *Mbp* and synaptophysin (*Syp*) were performed using 20  $\mu$ l of PCR MegaMix Blue (Client Life Science), 1  $\mu$ l of cDNA and 0.5  $\mu$ l of 10  $\mu$ M forward (F) and reverse (R) primers (Integrated DNA Technologies) in an ABI Veriti 96 Well thermal cycler (Thermo Fisher) for 30 cycles at 95°C, 72°C and 540°C: *Mbp*-F: GTGGTATGTGAGCACAGGCT; *Mbp*-R: TAAAAGCACCTGCTCTGGGG; *Syp*-F: TGCCATCTTCGCCTTTGCTA; *Syp*-R: GCCTGTCTCCTTGAACAGA.

Amplified products were loaded onto 1% E-Gel (Thermo Fisher) according to the manufacturer's instructions and imaged using an E-Gel imager (Thermo Fisher).

**Western blot and Coomassie staining for myelin and neuron protein from rat myelin preparations.** In brief, 15–20  $\mu$ g of protein were separated on 4–12% Bis-Tris NuPAGE gels (Thermo Fisher) according to the manufacturer's instructions. Gels were either stained for total protein using 0.3% w/v brilliant blue-G (Sigma-Aldrich) in 40% v/v methanol and 7% v/v glacial acetic acid overnight. Destaining was done with several washes in 40% v/v methanol and 7% v/v glacial acetic. For western blotting, proteins in gels were transferred onto PVDF membranes (Millipore Sigma) using Bolt transfer buffer (Thermo Fisher) for 1 h at 15 V constant voltage. Membranes were blocked with Li-Cor Blocking Buffer (Li-Cor) for 1 h at room temperature on a platform shaker. Membranes were incubated overnight in primary antibodies (1:2,000 dilution) rabbit anti-MBP (clone D8X4Q, Cell Signaling), rabbit anti-MOG (clone E5K6T, Cell Signaling), rabbit anti-neurofilament heavy (NF200, Millipore Sigma) or mouse anti-synaptophysin (clone SY38, Millipore Sigma) in 50% Li-Cor Blocking buffer in tris-buffered saline (TBS) with tween-20 (0.001% v/v) (TBS-T). Membranes were washed three times with TBS-T and Li-Cor 680-RD secondaries (1:5,000) (Li-Cor) applied in 50% v/v Li-Cor blocking buffer in TBS-T for 1 h at room temperature. Membranes were rinsed three times in TBS-T and imaged on a Li-Cor Odyssey (Li-Cor).

**Myelin enrichment assay and PCR.** Myelin enrichment of adult rat central nervous system was performed according to a previously published study<sup>51</sup>. Unless otherwise stated all buffers were prepared in DEPC-treated water and all procedures carried out at 4°C. In brief, adult rats were perfused with saline and the brains rapidly dissected, olfactory bulbs removed and kept on ice. Brains were cut into hemispheres, and one hemisphere was used for each preparation. Hemispheres were homogenized using a glass Dounce homogenizer in 6 ml of 0.32 M sucrose prepared in DEPC-treated water with HALT protease inhibitor cocktail without EDTA (Thermo Fisher). Then, 1 ml of homogenate was retained for further biochemical analysis and 6 ml of homogenate loaded on top of 6 ml of 0.85 M sucrose treated with DEPC-treated water with HALT protease inhibitors in 14-ml thin-walled centrifuge tubes (Beckman Coulter). Samples were centrifuged at 75,000 $g_{max}$  for 35 min at 4°C. The interface between 0.85 M and 0.32 M sucrose was collected, resuspended in water and centrifuged at 75,000 $g_{max}$  for 15 min at 4°C. The pellet was subjected to two rounds of osmotic shock by resuspension in water, left on ice for 10 min and centrifuged at 12,500 $g_{max}$  for 15 min at 4°C. The pellet was resuspended in 6 ml of 0.32 M sucrose and overlaid on a bed of 0.85 M sucrose and centrifuged at 75,000 $g_{max}$  for 35 min at 4°C. The purified myelin was collected from the 0.32 M–0.85 M sucrose interface. The myelin was then washed in 10 ml of water and centrifuged at 75,000 $g_{max}$  for 35 min at 4°C and resuspended in either 0.25 M bicarbonate pH 8.3 or TBS pH 7.4 to final volume of 400  $\mu$ l. Subsequently, 50  $\mu$ l was retained and 500  $\mu$ l of Tri-Reagent (Thermo Fisher) was added to preserve the RNA. Protein concentration was measured using BCA Protein Assay (Thermo Fisher) according to manufacturer's instructions.

**Animals used for myelin-microglia engulfment assays.** Wild-type C57BL/6J mice (stock no. 000664) were obtained from Jackson Laboratories. All animal experiments were carried out at the animal facility at the University of Massachusetts Medical School and approved (no. A-2496-17) by Animal Care and Use Committees (IACUC) and performed under NIH guidelines for proper animal welfare.

**Purification and treatment of primary mouse microglia.** Purified primary brain-derived microglia were obtained from mixed glial cultures by modified standard protocols as described<sup>52</sup>. In brief, cerebral cortices from male and female postnatal day 0.5 C57BL/6J wild-type mice were dissected free of meninges, chopped into small pieces and mechanically dissociated until a single-cell suspension was obtained. Cells were then seeded in 10 ml DMEM (Thermo Fisher) supplemented with 10% FBS (Thermo Fisher) and 1% penicillin–streptomycin (Thermo Fisher) at a density of one brain per 75 cm<sup>2</sup> flask, and cultured for 7 days at 37°C in humidified 5% CO<sub>2</sub>, 95% air. By shaking the culture flasks for 3 h at 180 r.p.m., loosely adhering microglia were detached. The suspended microglial cells were seeded onto glass coverslips at a density of 80,000 cells per well in a 24-well plate and cultured overnight. Subsequently, 24 h before treatment, cell culture medium was changed to neurobasal medium supplemented with 1  $\times$  sodium pyruvate, 1  $\times$  B27 (all from Thermo Fisher), 1  $\times$  GlutaMAX, 1  $\times$  penicillin–streptomycin (both from Thermo Fisher), 5  $\mu$ g/ml insulin, 1  $\times$  Sato supplement<sup>54</sup>,

5  $\mu$ g/ml *N*-acetyl-L-cysteine, 40 ng/ml T3 (all from Sigma-Aldrich), and 10 ng/ml mouse macrophage colony-stimulating factor (Shenandoah). Finally, microglia were treated with 6.45  $\mu$ g purified myelin fraction from rat brain for 4 h, before myelin was removed and cells were fixed or collected for analysis at the indicated time points. To visualize engulfment of myelin proteins into microglial lysosomes, myelin protein was labelled with pHrodo (Thermo Fisher) under RNase-free conditions according to the manufacturer's recommendations before treatment.

**Mbp RNA hybridization on primary mouse microglia.** RNA in situ hybridization was performed according to the manufacturer's recommendations (Biotechne). In brief, after treatment, cells were fixed with 4% PFA, dehydrated and stored at –20°C for up to 7 days before further use. Before RNA hybridization, cells were rehydrated, rinsed in PBS and treated with 1:15 diluted Protease III for 15 min at 40°C. Then, probes against *Mbp* (Biotechne) were added and incubated for 2 h at 40°C. Subsequent amplification steps were performed according to the manufacturer's instructions. To confirm specificity of RNA signals, some samples were treated with 10 mg/ml RNaseA (Thermo Fisher) for 1 h at 37°C before incubation with probes. To immunostain samples following *Mbp* RNA hybridization, cells were washed in PBS, blocked in 2% normal goat serum supplemented with 0.01% Triton X-100 for 30 min and incubated with the following primary antibodies: rabbit polyclonal anti-Iba1 (Wako Chemicals) and rat monoclonal anti-CD68 (clone FA-11, Bio-Rad) (both 1:100). The following day, cells were incubated with appropriate Alexa Fluor-conjugated secondary antibodies (Thermo Fisher) and mounted with Vectashield containing DAPI (Vector). Random 63 $\times$  fields of all cultures were imaged using identical settings on a Zeiss Observer Spinning Disk Confocal microscope equipped with diode lasers (405 nm, 488 nm, 594 nm, 647 nm) and Zen Blue acquisition software (Zeiss). For unbiased quantification of *Mbp* puncta, signals were co-localized to Iba1<sup>+</sup> microglia, the investigator was blinded to treatment of the samples and the number of total puncta as well as signals associated with microglia nuclei (0.5  $\mu$ m distance from the nucleus) were determined using ImageJ software (NIH). Moreover, 630 $\times$  z-stacks were acquired with 35–50 steps at 0.22  $\mu$ m spacing and processed in Imapris (Bitplane) to three-dimensional surface render engulfed signals as previously described<sup>53</sup>.

**RNA isolation and quantitative PCR with reverse transcription.** Total RNA from microglia was extracted using TRIzol (Thermo Fisher) according to manufacturer's recommendations. Then, 500 ng of total RNA was transcribed into cDNA using Power SYBR Green Cells-to-CT Kit (Thermo Fisher) according to the manufacturer's instructions. Relative *Cd163* and *P2ry12* expression was determined by quantitative PCR in relation to *Gapdh* housekeeping gene expression using the following forward (F) and reverse (R) primers (Integrated DNA Technologies): *Cd163*-F: GGGTCATTCAGAGGCACACTG; *Cd163*-R: CTGGTCTGCCTGTCAAGGCT; *P2ry12*-F: GTTCTACGTGAAGGAGAGCA; *P2ry12*-R: CTACATTGGGGTCTCTCGC; *Gapdh*-F: TGTCCGTCGTGGATCTGAC; *Gapdh*-R: CCTGCTTACCACCTTCTTG.

**Human tissue sampling for primary human microglia assays.** Human brain tissue was obtained with informed consent under protocol REC 16/LO/2168 approved by the NHS UK Health Research Authority. Adult human brain tissue was obtained from three biopsies (age 17, male, diffuse axonal injury, right frontal lobe; age 61, male, unruptured cerebral aneurysm, right gyrus rectus; age 70, male, normal pressure hydrocephalus, right parietal lobe) taken from the site of neurosurgery resection for the original clinical indication. Tissue was transferred to Hibernate A low fluorescence (HALF) supplemented with 1  $\times$  SOS (Cell Guidance Systems), 2% Glutamax (Thermo Fisher), 1% penicillin–streptomycin, 0.1% BSA, DNase 1 type IV (40 g/ml), insulin (4g/ml, all Sigma-Aldrich) and pyruvate (220 g/ml, Gibco) on ice and transported to a dedicated BCL 2 laboratory.

**Dissociation of human brain tissue and purification of human microglia.** Brain tissue was mechanically digested in fresh ice-cold HALF supplemented with 1  $\times$  SOS (Cell Guidance Systems), 2% Glutamax (Thermo Fisher), 1% penicillin–streptomycin, 0.1% BSA, DNase 1 type IV (40 g/ml), insulin (4 g/ml, all Sigma-Aldrich) and pyruvate (220 g/ml, Gibco). The prepared mix was spun in HBSS+ (Thermo Fisher) at 300g for 5 min and supernatant was discarded. The digested tissue was rigorously triturated at 4°C and filtered through a 70- $\mu$ m nylon cell strainer (Falcon) to remove large cell debris and undigested tissue. Filtrate was spun in a 22% Percoll gradient with DMEM F12 (both Sigma-Aldrich) at 800g for 20 min. Supernatant was discarded and the pellet was resuspended in ice-cold supplemented HALF. The isolated cell suspension was incubated with anti-CD11b conjugated magnetic beads (Miltenyi) for 15 min at 4°C. Cells were washed twice with supplemented HALF and passed through an MS column (Miltenyi). Each sample was washed three times in the column and then extracted. Cells were plated in DMEM F12 with 10% FBS and 0.1% macrophage colony-stimulating factor. Note that all cell culture incubators are regularly tested for mycoplasma contamination.

**Mbp and Plp1 RNA hybridization on primary human microglia.** Purified rat brain myelin extracts from three biological replicates were diluted to 1 mg/ml (total protein) in 0.1 M sodium bicarbonate buffer, pH 8.3 in a volume of 100  $\mu$ l. The pH-sensitive fluorescent dye succinimidyl ester known as pHrodoRed

(Thermo Fisher) was added from a 10 mM stock in DMSO to a final concentration of 100  $\mu$ M to each myelin extract for 45 min at room temperature. Samples were centrifuged for 30 min at 17,000g at 4°C and the supernatant was discarded. The labelled myelin pellets were resuspended in 100  $\mu$ l of 0.1 M sodium bicarbonate buffer, pH 8.3 to a final concentration of 1mg/ml of protein and 1.5  $\mu$ l was added to wells of human microglia in 24-well glass bottom plate (Cellvis) for phagocytosis over 18 h. The next day, the cells were washed twice with PBS before fixation with 4% PFA at room temperature for 10 min and washing with PBS.

Cells were manually stained for RNA using RNAScope using a modified automated procedure for the Leica Bond RX (Leica). Fixed cells were washed twice with Bond wash solution (Leica) before antigen retrieval with Bond Epitope Retrieval Solution 2 (Leica) at 95°C and allowed to cool to room temperature, and followed by three washes with Bond wash. Cells were permeabilized with 0.5 $\times$  RNAScope 2.5 LS Protease III (Biotechne) in PBS at 37°C for 5 min, followed by cold Bond wash (40°C) and then two more Bond washes at room temperature. Endogenous peroxidase activity was quenched with RNAScope 2.5 LS Hydrogen Peroxide (Biotechne) for 10 min and followed by two more Bond washes. RNAScope probes for mouse *Mbp* (Biotechne) and *Plp1* (Biotechne) were diluted 1:50 in C1 probe. *Mbp* and *Plp1* probes were amplified using sequential treatments with RNAScope LS Multiplex AMP 1, 2 and 3 (Biotechne) for 30 min at 42°C with Bond washing and RNAScope 2.5 LS Rinse Reagent (Biotechne) for 5 min each between each amplification step. Probe channel C2 for *Mbp* was fluorescently developed using RNAScope Multiplex HRP-C2 (Biotechne) for 15 min at 42°C, followed by Bond washes and incubation with tyramide-conjugated Opal 520 dye at 1:2,500 (Perkin Elmer) for 30 min followed with two more BOND washes. Residual HRP activity was quenched with RNAScope LS Multiplex HRP Blocker (Biotechne) for 15 min at 42°C, followed by Bond washes. Probe channel C3 for *Plp-1* was developed as for C2 but using RNAScope LS Multiplex HRP-C3 (Biotechne) and Opal 650 dye at 1:2,500 (Perkin Elmer) and followed by RNAScope LS Multiplex HRP Blocker (Biotechne) with Bond washing. Staining of LMNA/C (lamin A/C) was done after RNAScope development by incubating cells with mouse anti-porcine lamin A/C antibody (Insight Biotechnology) at 1:200 and rabbit anti-Iba1 biotin-conjugated antibody at 1:200 for 60 min at room temperature. Excess primary antibodies were washed away with Bond wash and cells incubated goat anti-mouse IgG2B AlexaFlour 350 at 1:500 and streptavidin-conjugated AlexaFlour 700 at 1:1,000 for 60 min at room temperature. Cells were washed three times in Bond wash and twice in PBS before imaging on an Operetta CLS (Perkin Elmer) spinning disk confocal microscope.

**Image acquisition and analysis of human immunohistochemistry and in situ hybridization experiments.** Bright field images were acquired on Zeiss Axio Imager 2 and Leica DMI8 microscopes equipped with Zeiss AxioCam 512 colour and Leica DMC5400 cameras. Fluorescence images were taken using Leica TCS SP8 and TCS SPE laser confocal and DMI8 wide field (equipped with Leica DFC7000 GT camera) microscopes with 10 $\times$ , 20 $\times$ , 40 $\times$  or 63 $\times$  objectives; all fluorescent confocal pictures are z-stack images unless stated otherwise. High-resolution FISH images of human tissue sections were acquired on a spinning disk Operetta CLS (Perkin Elmer) in confocal mode using a sCMOS camera and a 40 $\times$  1.1 numerical aperture automated water-dispensing objective. The field of view was 320  $\times$  320  $\mu$ m and voxel size 0.3  $\times$  0.3  $\times$  1  $\mu$ m. Each field was imaged as a z-stack consisting of 20 to 30 planes with a 1  $\mu$ m step size. z-heights of tissue sections were manually identified by imaging DAPI on sample fields before tissue-wide scans. Each z plane was imaged across 5 channels depending on the experiment with exposure between 60 and 120 ms at 90% LED power. Three-dimensional projections were generated using raw imaging data in Volocity 6.3 software (Perkin Elmer). Images were processed using Fiji ImageJ v.2.0 (NIH) or Photoshop software (Adobe) and exported to Illustrator vector-based software (Adobe) for figure generation.

**Statistical analysis.** Data are presented as mean  $\pm$  s.e.m. Analyses were performed using two-tailed parametric or non-parametric (Mann–Whitney, Kruskal–Wallis) *t*-tests for two groups and if applicable, one-way ANOVA with corresponding post hoc tests for multiple group comparisons. *P* values were designated as follows: \**P*  $\leq$  0.05, \*\**P*  $\leq$  0.01, \*\*\**P*  $\leq$  0.001 and \*\*\*\**P*  $\leq$  0.0001. Statistical analyses and graphical visualizations were performed using GraphPad Prism (GraphPad Software) and open-source R programming software (<https://www.r-project.org>).

**Reporting summary.** Further information on research design is available in the Nature Research Reporting Summary linked to this paper.

## Data availability

All raw snRNA-seq data (fastq files) were deposited to the Sequence Read Archive (SRA) under accession number PRJNA544731 (NCBI Bioproject ID: 544731).

42. Matevosian, A. & Akbarian, S. Neuronal nuclei isolation from human postmortem brain tissue. *J. Vis. Exp.* **20**, e914 (2008).
43. Shekhar, K. et al. Comprehensive classification of retinal bipolar neurons by single-cell transcriptomics. *Cell* **166**, 1308–1323 (2016).
44. Maaten, L. d. & Hinton, G. Visualizing data using t-SNE. *J. Mach. Learn. Res.* **9**, 2579–2605 (2008).
45. Finak, G. et al. MAST: a flexible statistical framework for assessing transcriptional changes and characterizing heterogeneity in single-cell RNA sequencing data. *Genome Biol.* **16**, 278 (2015).
46. Love, M. I., Huber, W. & Anders, S. Moderated estimation of fold change and dispersion for RNA-seq data with DESeq2. *Genome Biol.* **15**, 550 (2014).
47. Trapnell, C. et al. The dynamics and regulators of cell fate decisions are revealed by pseudotemporal ordering of single cells. *Nat. Biotechnol.* **32**, 381–386 (2014).
48. Yu, G., Wang, L.-G., Han, Y. & He, Q.-Y. clusterProfiler: an R package for comparing biological themes among gene clusters. *OMICS* **16**, omi.2011.0118 (2014).
49. Aibar, S. et al. SCENIC: single-cell regulatory network inference and clustering. *Nat. Methods* **14**, 1083–1086 (2017).
50. Meguro, R. et al. Nonheme-iron histochemistry for light and electron microscopy: a historical, theoretical and technical review. *Arch. Histol. Cytol.* **70**, 1–19 (2007).
51. Jahn, O., Tenzer, S., Bartsch, N., Patzig, J. & Werner, H. B. In *The Cytoskeleton* (ed. Dermietzel, R.) 335–353 (Humana, 2013).
52. Werneburg, S., Mühlenhoff, M., Stangel, M. & Hildebrandt, H. Polysialic acid on SynCAM 1 in NG2 cells and on neuropilin-2 in microglia is confined to intracellular pools that are rapidly depleted upon stimulation. *Glia* **63**, 1240–1255 (2015).
53. Schafer, D. P. et al. Microglia sculpt postnatal neural circuits in an activity and complement-dependent manner. *Neuron* **74**, 691–705 (2012).
54. Chen, Y. et al. NS21: re-defined and modified supplement B27 for neuronal cultures. *J. Neurosci. Methods* **171**, 239–247 (2008).

**Acknowledgements** We thank J. Cyster (UCSF), D. Reich (National Institutes of Health, Bethesda) and S. Teichmann (Wellcome Sanger Institute) for advice and comments on the manuscript, I. Pshenichnaya for technical assistance and A. Hupalowska for figure illustrations. D. Gveric and A. LeFevre provided human brain samples from the UK Multiple Sclerosis Tissue Bank, funded by the Multiple Sclerosis Society of Great Britain and Northern Ireland, and the National Institutes of Health (NIH) NeuroBioBank at the University of Maryland, respectively. L.S. was supported by postdoctoral fellowships from the German Research Foundation (DFG, SCHI 1330/1-1) and the National Multiple Sclerosis Society (NMSS) funded in part by the Dave Tomlinson Research Fund (FG-1607-2511). D.V. was supported by a BOLD & BASIC fellowship from the UCSF Quantitative Biosciences Institute. S.W. was supported by a postdoctoral fellowship from the DFG (WE 6170/1-1), and S.M. was supported by EMBO (ALTF\_393-2015) and DFG (MA 7374/1-1). A.B. acknowledges an NIH postdoctoral fellowship (F32NS103266). D.H.R. is a Paul G. Allen Frontiers Group Distinguished Investigator. This work was funded by the Dr. Miriam and Sheldon G. Adelson Medical Research Foundation (D.H.R., D.P.S., R.J.M.F.), the Hertie Foundation (medMS-MyLab program; P1180016 to L.S.), the National Human Genome Research Institute (4U41HG002371 to M.H.), the California Institute for Regenerative Medicine (GC1R-06673-C to M.H.), the Silicon Valley Community Foundation (2018-182809 to M.H.), the NMSS (PP-1609-25953 to D.H.R.), the NIHR Cambridge Biomedical Research Center (D.H.R.), and grants from the NIH/NINDS (NS040511 to D.H.R., R35NS097305 to A.R.K.), European Research Council and the Wellcome Trust (to D.H.R.).

**Author contributions** L.S., D.V., A.R.K. and D.H.R. designed, coordinated and interpreted all studies and wrote the manuscript. L.S. and R.R. selected control and MS samples. L.S., D.V. and D.J. performed snRNA-seq assisted by B.T. and N.G. D.V. and M.K. performed regression and trajectory analysis of single-cell data, assisted by A.B. and J.B.E., who modified analytical scripts with oversight from M.A.F., A.R.K. and D.H.R. S.H., L.S., D.J., S.V. and S.M. performed smFISH with oversight from O.A.B. and L.R.S. S.W., J.H.S., A.Y. and M.S. conducted mouse and human myelin–microglia engulfment assays and analysis, supervised by D.P.S. and R.J.M.F. L.S. and L.R.S. analysed findings related to immune cells. M.H. generated the single-cell web browser to visualize control and MS sequencing data. All coauthors read, revised and approved the manuscript. D.H.R. and A.R.K. supervised all experiments.

**Competing interests** The authors declare no competing interests.

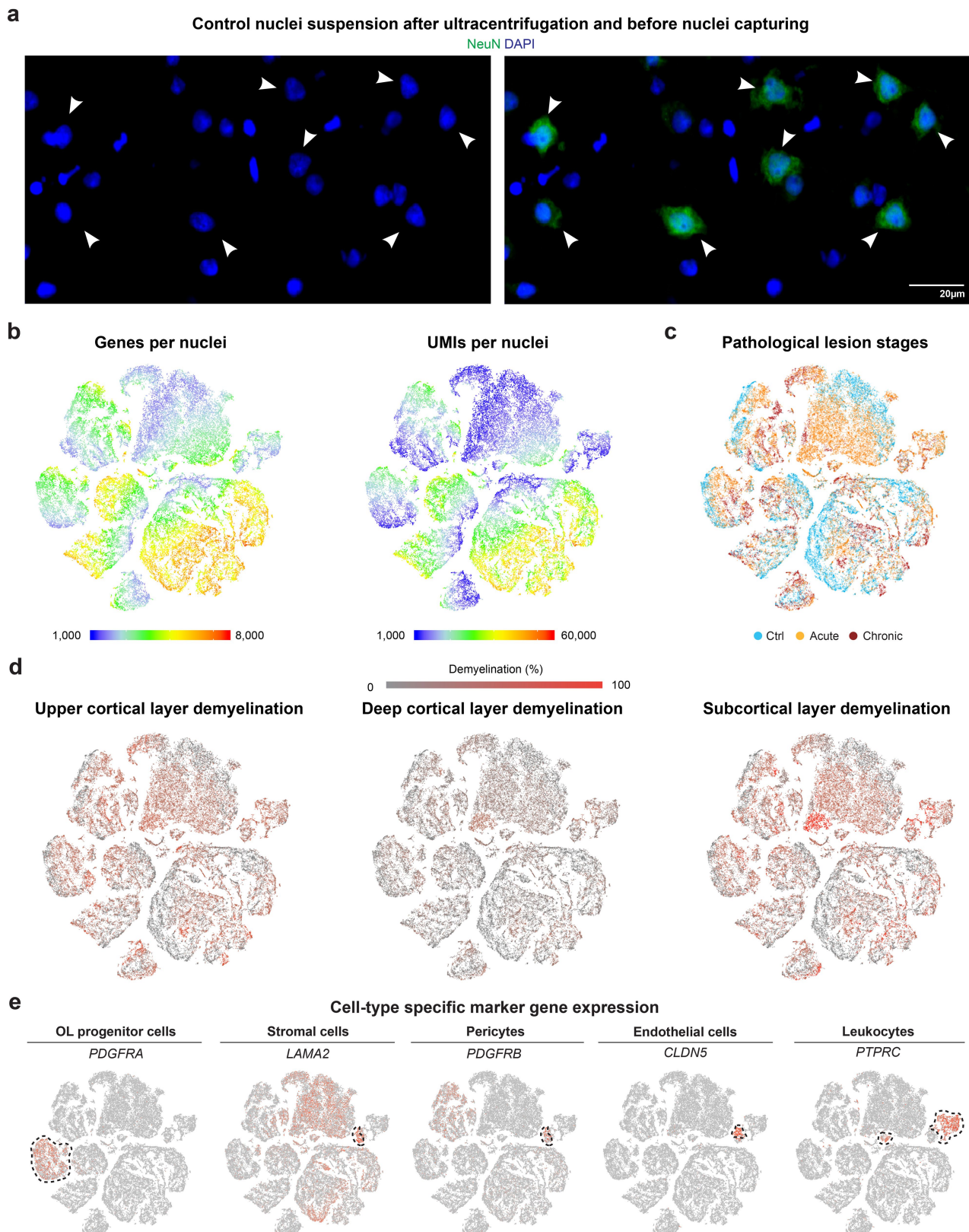
## Additional information

**Supplementary information** is available for this paper at <https://doi.org/10.1038/s41586-019-1404-z>.

**Correspondence and requests for materials** should be addressed to A.R.K. or D.H.R.

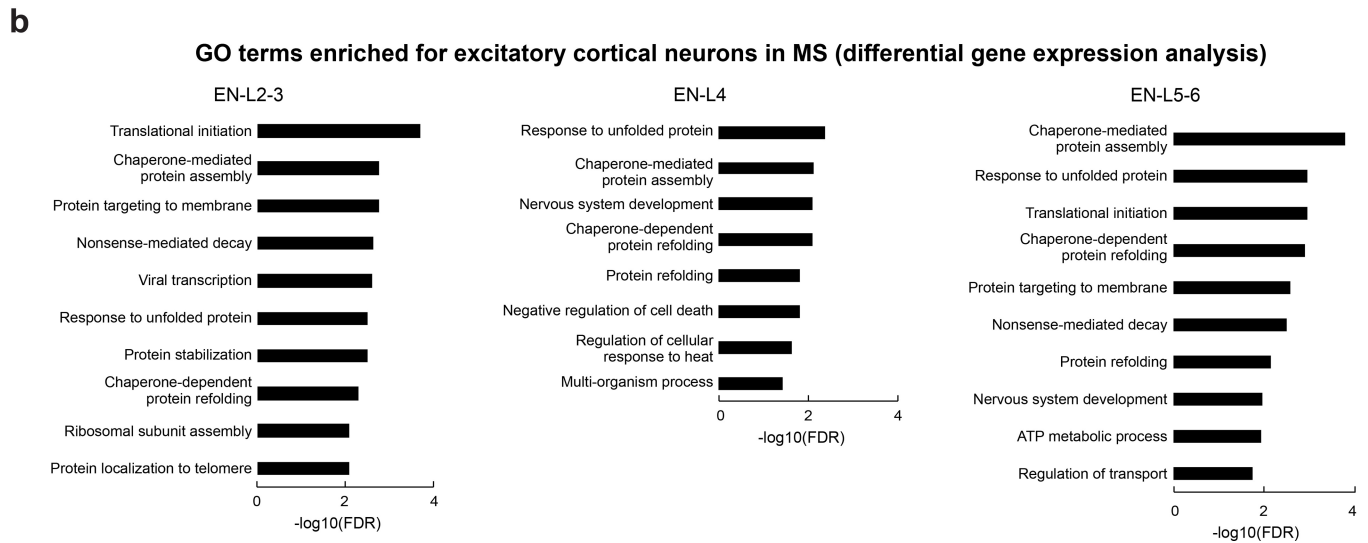
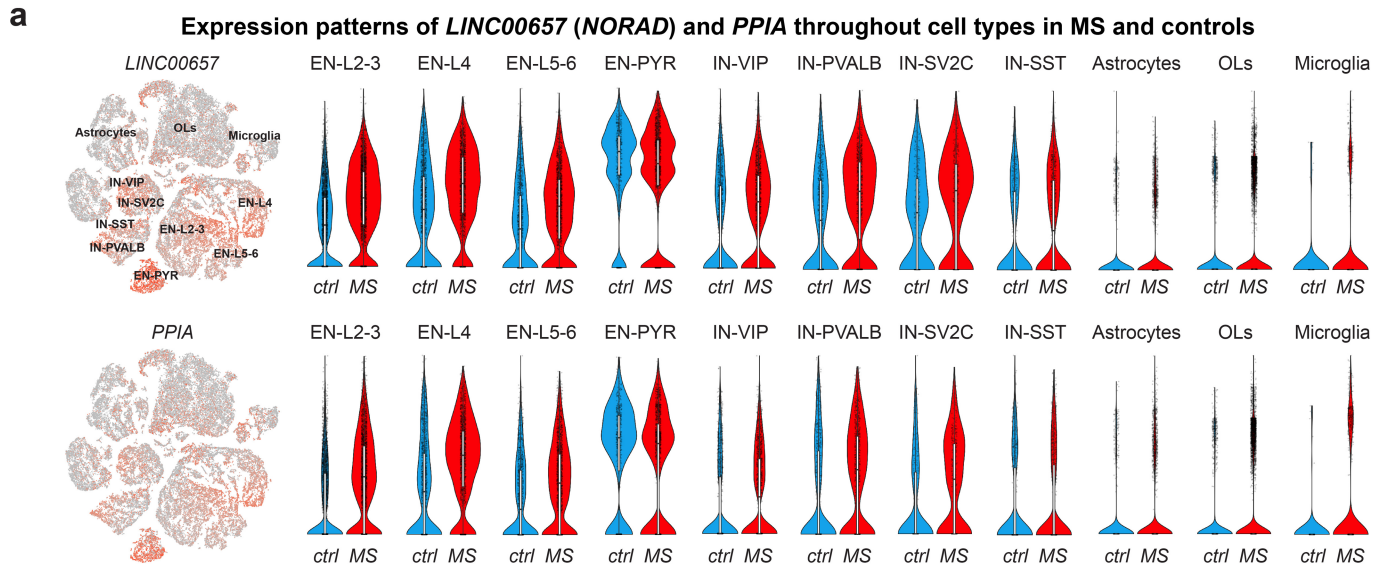
**Peer review information** *Nature* thanks Marco Prinz, Ori Staszewski and theother anonymous reviewer(s) for their contribution to the peer review of this work.

**Reprints and permissions information** is available at <http://www.nature.com/reprints>.



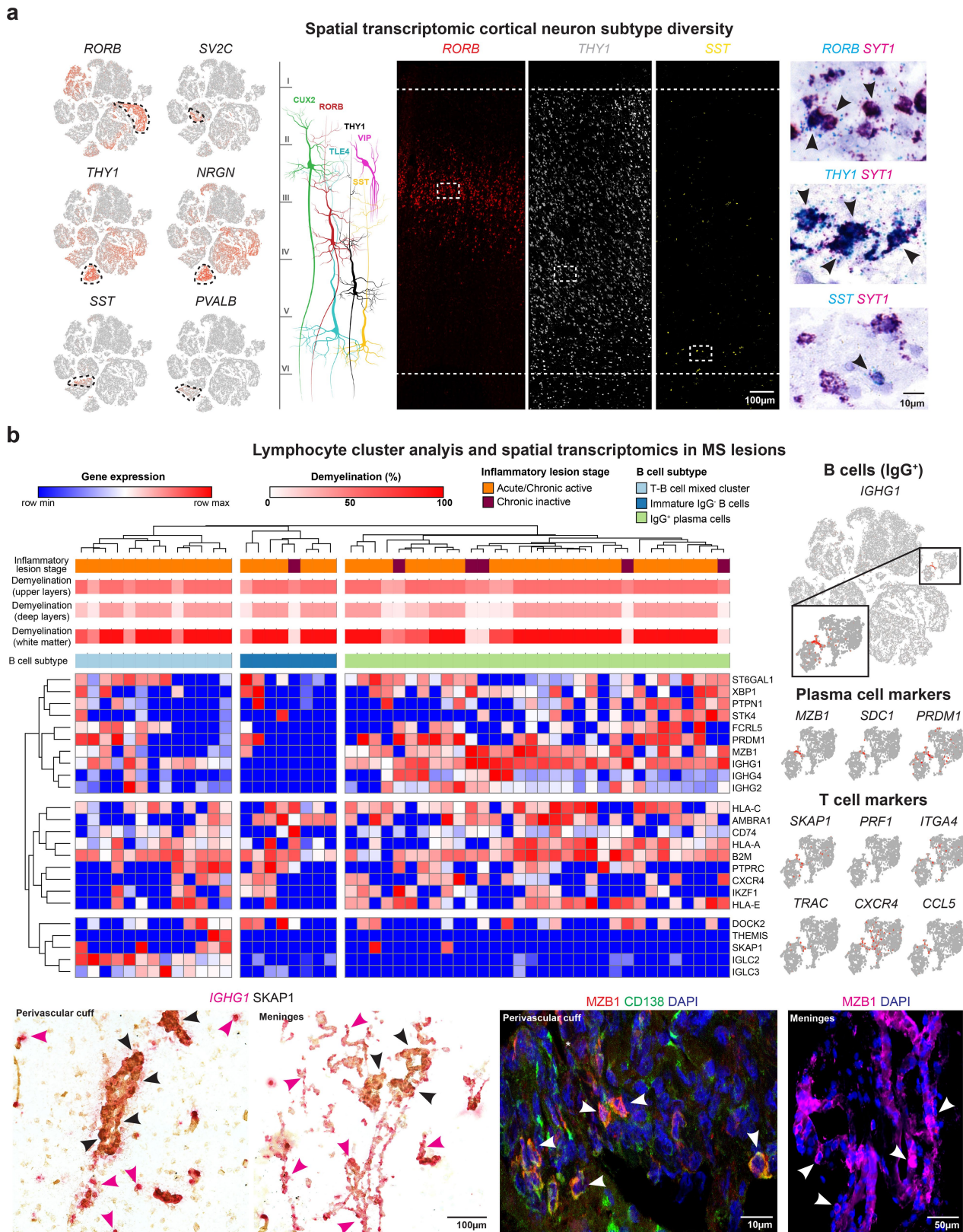
**Extended Data Fig. 1 | Sample and disease contribution of cell types captured by snRNA-seq.** **a**, Representative images selected from nuclear suspensions (control,  $n = 9$ ) after ultracentrifugation and before capturing by 10x Genomics confirming DAPI nuclear counterstaining with presence of smaller and larger DAPI<sup>+</sup> nuclei. Note that larger nuclei are co-stained with anti-NeuN antibody confirming neuronal origin (white arrowheads). **b**, Coloured *t*-SNE plots showing numbers of genes (left) and UMIs (right) per captured nuclei from control and MS samples. **c**, Coloured *t*-SNE plot

visualizing nuclei from different lesion stages based on classic pathological MS lesion staging. Acute, acute chronic-active; chronic, chronic inactive; ctrl, control. **d**, Coloured *t*-SNE plots visualizing nuclei from samples with different levels of upper- and deep-layer cortical demyelination as well as subcortical demyelination. **e**, Representative *t*-SNE plots with cell-type specific marker genes for OL progenitor cells, stromal cells including pericytes, endothelial cells and leukocytes. For *t*-SNE plots, data shown from 9 control and 12 MS samples and a total of 48,919 nuclei.



**Extended Data Fig. 2 | Molecular changes in cortical neuron subtypes in MS lesions.** **a**, *NORAD* and *PPIA* expression patterns in cortical neurons and selected glial subtypes. Note baseline expression of *NORAD* and *PPIA* in neuronal versus glial subtypes and preferential upregulation of both *NORAD* and *PPIA* in upper-cortical-layer ENs (L2–L3 EN (EN-L2-3) and L4 EN (EN-L4)) in MS lesion tissue versus deep-cortical-layer excitatory and inhibitory neurons (L5–L6 EN (EN-L5-6) and IN-SST). For all *t*-SNE and violin plots, data are shown from 9 control and 12 MS samples. For *t*-SNE plots, data from 48,919 nuclei are shown.

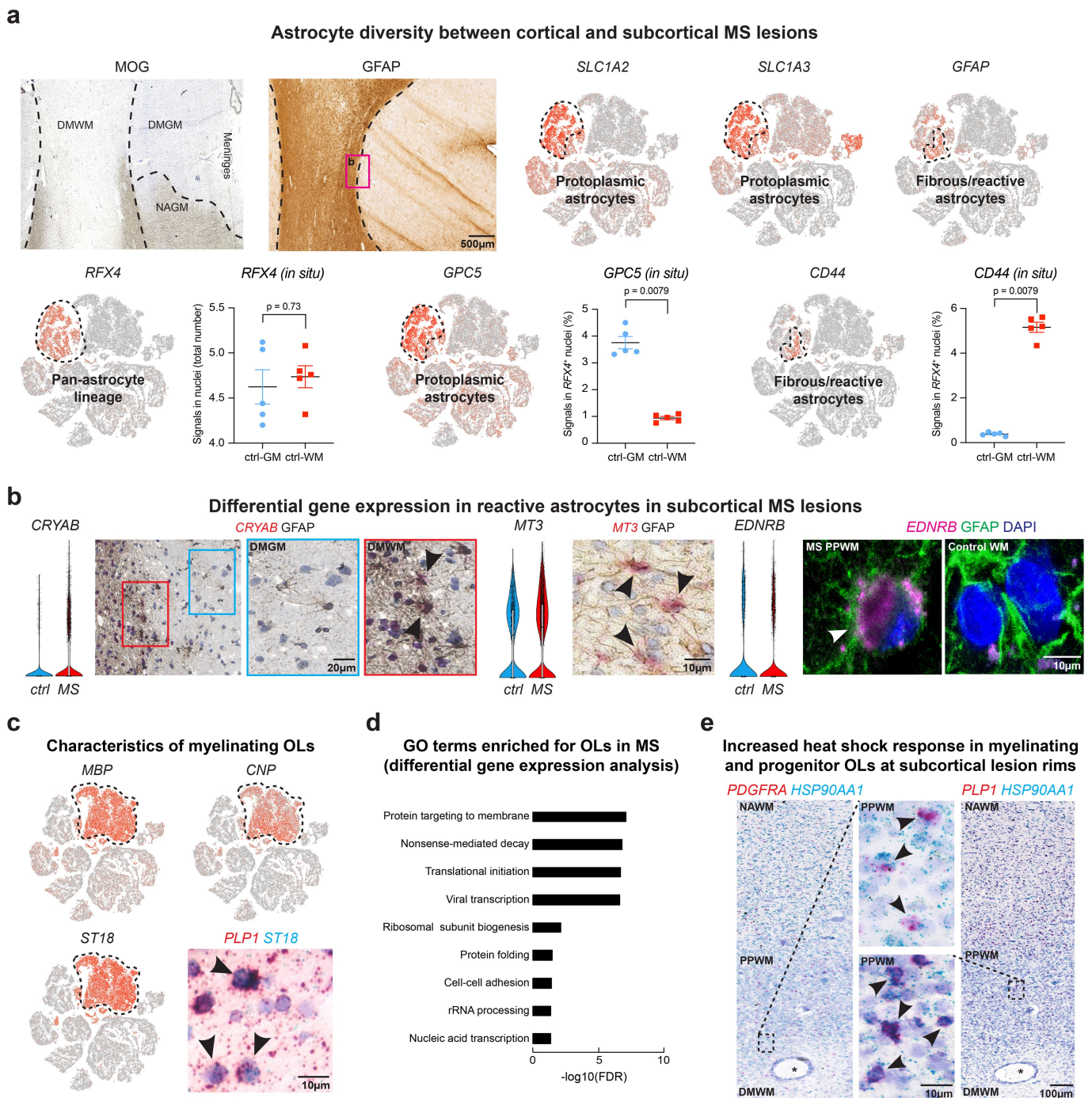
For L2–L3 EN, L4 EN and L5–L6 EN violin plots, data are shown from 6,120, 3,125 and 3,058 nuclei. Box plots inside violin plots represent median and standard deviation of gene expression. **b**, Visualization of enriched GO terms in L2–L3 EN, L4 EN and L5–L6 EN cells based on DGE analysis (linear mixed model regression). Binomial test with FDR correction was used to calculate FDR-corrected *P* values using genes differentially expressed in L2–L3 EN, L4 EN and L5–L6 EN nuclei ( $n = 428, 364$  and  $327$ , respectively).



Extended Data Fig. 3 | See next page for caption.

**Extended Data Fig. 3 | Cortical neuron and lymphocyte subtype analysis in MS lesions.** **a**, *t*-SNE plots for neuron subtype specific expression of *RORB*, *THY1*, *NRGN*, *SST*, *SV2C* and *PVALB* (left). LAST (control,  $n = 5$ ) showing layer-specific expression of neuronal *RORB* in intermediate cortical layer 4 and widespread expression of pyramidal neuron marker *THY1* with enrichment in layer 5; note that *SST*-expressing INs preferentially map to deep-cortical layers. Co-expression studies (control,  $n = 5$ ) with *SYT1* confirm neuronal expression of *RORB*, *THY1* and *SST* (black arrowheads). **b**, Heat map with hierarchical clustering of lymphocyte-associated transcripts allowing subclustering of lymphocytes in T cells, B cells and plasma cells based on marker gene expression (top left). *t*-SNE plots for typical B cell (plasma cell) and T cell marker genes enriched in lymphocyte clusters (top right). Immunohistochemistry for T cell adapter protein SKAP1 (black arrowheads mark SKAP1<sup>+</sup> T cells)

together with spatial transcriptomics for B-cell-associated *IGHG1* encoding immunoglobulin G1 (IgG1) (magenta arrowheads; bottom left); note increased expression of the plasma cell-associated marker gene *MZB1* (top left) and preferential enrichment of MZB1<sup>+</sup> and *IGHG1*-expressing plasma cells (white arrowheads, bottom right) in inflamed meningeal tissue versus mixed T and B cell infiltration in perivascular cuffs of subcortical lesions (bottom). One caveat to these findings is the relatively small number of MS tissue samples, which limited our ability to cluster T cell populations. For *t*-SNE plots (**a**, **b**) and hierarchical clustering (**b**), data are shown from 9 control and 12 MS samples. For *t*-SNE plots, data shown for all 48,919 nuclei; for hierarchical clustering, data are shown from 53 nuclei in the B cell cluster. For in situ hybridization and immunohistochemistry experiments in **b**, representative images shown from individual tissue sections (control,  $n = 4$ ; MS,  $n = 7$ ).

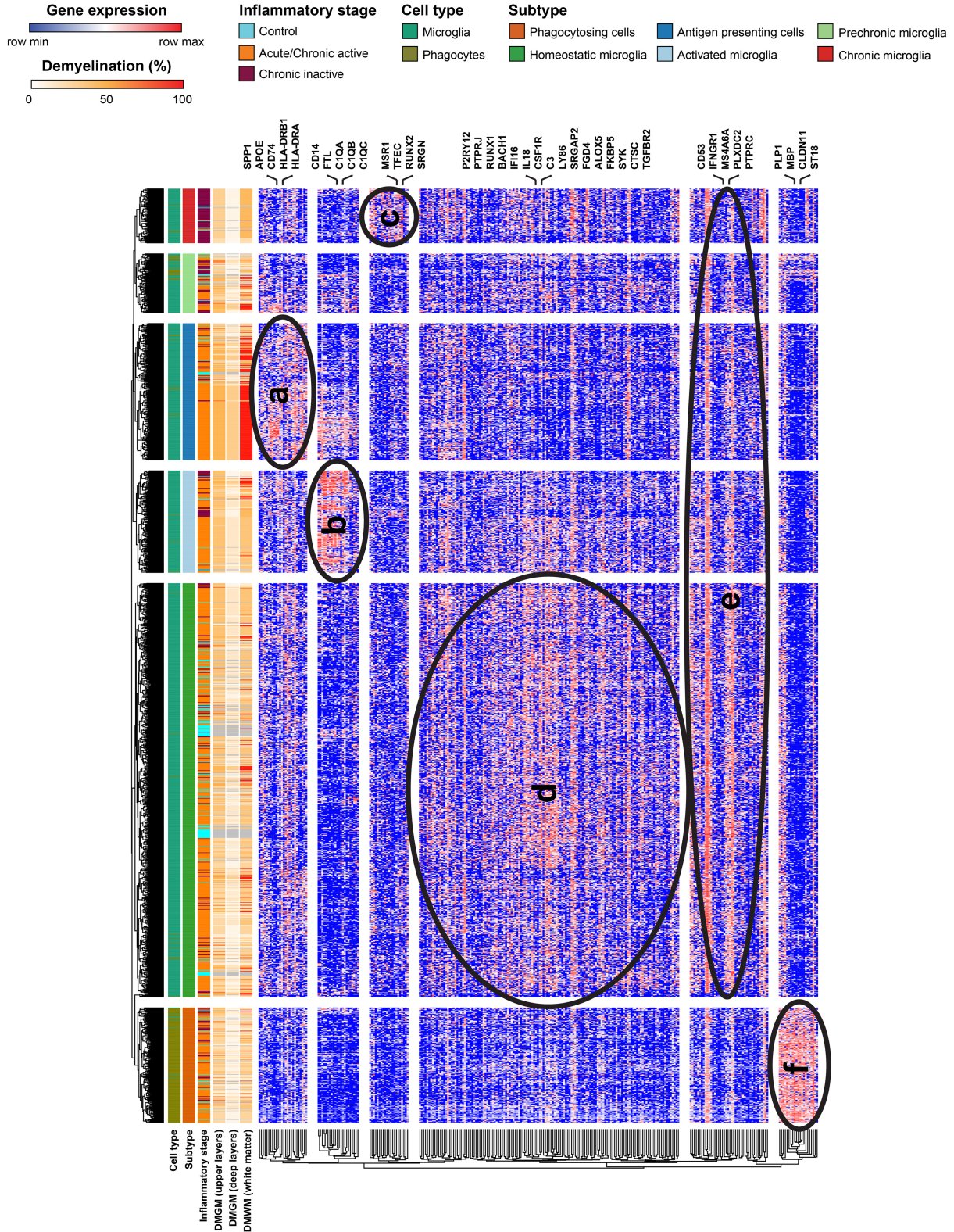


#### Extended Data Fig. 4 | Astrocyte and oligodendrocyte cluster analysis and spatial transcriptomics in MS lesions.

**a**, Differential spatial expression patterns of astroglial GFAP in subcortical versus cortical demyelination by immunohistochemistry (left); *t*-SNE plots visualizing astrocyte-specific genes corresponding to all (*RFX4*), protoplasmic (*SLC1A2*, *GPC5*) and fibrous or reactive astrocytes (*GFAP*, *CD44*). Quantification of *RFX4*<sup>+</sup> in situ hybridization signals per nuclei in GM and WM of control samples validates *RFX4* as a canonical astrocyte marker (control,  $n = 5$ ); quantification of *GPC5*<sup>+</sup> and *CD44*<sup>+</sup> in situ hybridization signals per *RFX4*<sup>+</sup> astrocytes validates *GPC5* as protoplasmic GM and *CD44* as fibrous WM marker. Two-tailed Mann–Whitney *U*-tests were performed. Data are mean  $\pm$  s.e.m. **b**, Upregulation of astroglial *CRYAB*, *MT3* (black arrowheads) and endothelin type B receptor transcript *EDNRB* (white arrowhead) in reactive astrocytes in subcortical lesions. **c**, *t*-SNE plots showing OL-specific expression of

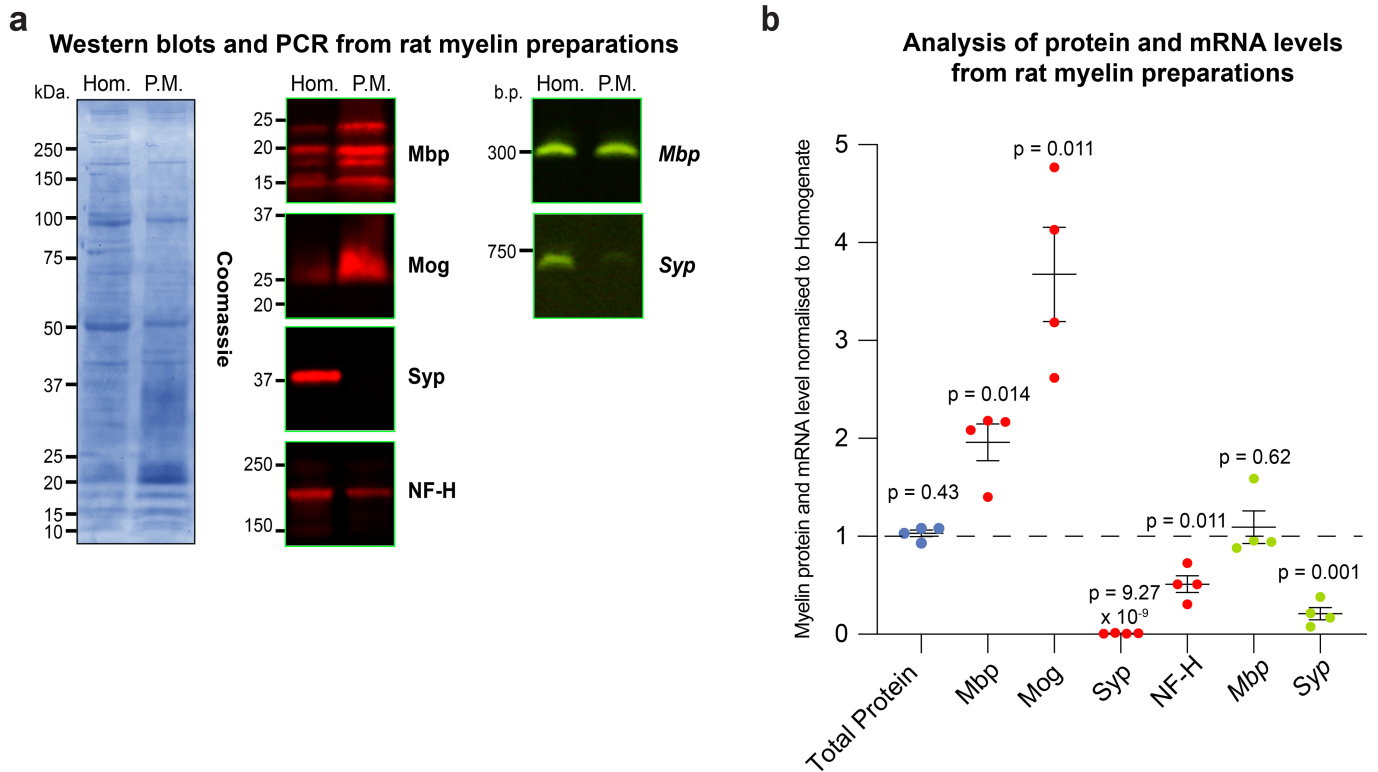
myelin-encoding genes *MBP*, *CNP* and transcription factor *ST18*; note co-expression of *ST18* with *PLP1* in control WM by in situ hybridization. **d**, Visualization of enriched GO terms in myelinating OLs based on DGE analysis. Binomial test with FDR correction was used to calculate FDR-corrected *P* values using 151 genes differentially expressed in OLs. **e**, Co-expression spatial transcriptomic studies confirming upregulation of heat-shock protein 90 transcript *HSP90AA1* in both progenitor (*PDGFRA*-expressing) and myelinating (*PLP1*-expressing) OLs at lesion rims (PPWM, black arrowheads). The black asterisk indicates a blood vessel. For *t*-SNE and violin plots, data shown from 9 control and 12 MS samples. For astrocyte violin plots, data shown from 1,571 control and 3,810 MS nuclei are shown. Box plots inside violin plots represent median and standard deviation of gene expression. For in situ hybridization and immunohistochemistry experiments, representative images from from three control and four MS individual tissue sections are shown.

Microglia hierarchical cluster analysis



**Extended Data Fig. 5 | Cluster analysis of activated and phagocytosing microglia subtypes.** Hierarchical cluster analysis identifies several homeostatic and activated MS-specific microglia subtypes according to inflammatory lesion stages allowing transcriptomic staging of microglia

subtypes. Clusters with enriched genes are marked and annotated a-f (see Supplementary Table 7 for gene list). Note that phagocytosing cells are identified by presence of OL and myelin-associated encoded genes (cluster f at the bottom of the heat map).



**Extended Data Fig. 6 | PCR for rat *Mbp* from myelin preparation.**

**a**, Representative Coomassie stain of brain homogenate (Hom.) and purified myelin (P.M.) from adult rat brain (left). Western blots for myelin basic protein (Mbp), Mog, synaptophysin (Syp) and neurofilament heavy molecular weight (NF-H) (centre). PCRs of myelin basic protein (*Mbp*) and synaptophysin (*Syp*) transcripts in brain homogenate and purified myelin fractions (right). **b**, Densitometric quantification of myelin and

homogenates prepared from  $n = 4$  independent rat hemispheres for Coomassie (total protein), western blot proteins and PCRs shown in **a** of purified myelin fractions normalized to their respective homogenates. Data are median  $\pm$  s.e.m. of the four biological replicates. Similar results were obtained with brain homogenate and purified myelin fractions not used in this study. *P* values were calculated from Student's two tailed *t*-test with Welch's correction.  $P < 0.05$  was considered significant.

## Reporting Summary

Nature Research wishes to improve the reproducibility of the work that we publish. This form provides structure for consistency and transparency in reporting. For further information on Nature Research policies, see [Authors & Referees](#) and the [Editorial Policy Checklist](#).

### Statistics

For all statistical analyses, confirm that the following items are present in the figure legend, table legend, main text, or Methods section.

n/a Confirmed

- The exact sample size ( $n$ ) for each experimental group/condition, given as a discrete number and unit of measurement
- A statement on whether measurements were taken from distinct samples or whether the same sample was measured repeatedly
- The statistical test(s) used AND whether they are one- or two-sided  
*Only common tests should be described solely by name; describe more complex techniques in the Methods section.*
- A description of all covariates tested
- A description of any assumptions or corrections, such as tests of normality and adjustment for multiple comparisons
- A full description of the statistical parameters including central tendency (e.g. means) or other basic estimates (e.g. regression coefficient) AND variation (e.g. standard deviation) or associated estimates of uncertainty (e.g. confidence intervals)
- For null hypothesis testing, the test statistic (e.g.  $F$ ,  $t$ ,  $r$ ) with confidence intervals, effect sizes, degrees of freedom and  $P$  value noted  
*Give  $P$  values as exact values whenever suitable.*
- For Bayesian analysis, information on the choice of priors and Markov chain Monte Carlo settings
- For hierarchical and complex designs, identification of the appropriate level for tests and full reporting of outcomes
- Estimates of effect sizes (e.g. Cohen's  $d$ , Pearson's  $r$ ), indicating how they were calculated

*Our web collection on [statistics for biologists](#) contains articles on many of the points above.*

### Software and code

Policy information about [availability of computer code](#)

Data collection

No code was used for data collection

Data analysis

For snRNA-seq analysis, the following software and packages have been used: Illumina bcl2fastq v2.19, Cell Ranger v1.3; svd from base package v3.6.0, igraph 1.0.1, MAST v1.10.0 (R packages); MulticoreTSNE v1.0.0 (Python module), PANTHER v14.0, DESeq2 version 1.20.0, Monocle v3, clusterProfiler package version 3.10.1, Morpheus software, Fiji ImageJ v2.0.

For manuscripts utilizing custom algorithms or software that are central to the research but not yet described in published literature, software must be made available to editors/reviewers. We strongly encourage code deposition in a community repository (e.g. GitHub). See the Nature Research [guidelines for submitting code & software](#) for further information.

### Data

Policy information about [availability of data](#)

All manuscripts must include a [data availability statement](#). This statement should provide the following information, where applicable:

- Accession codes, unique identifiers, or web links for publicly available datasets
- A list of figures that have associated raw data
- A description of any restrictions on data availability

SRA accession number: PRJNA544731 (NCBI Bioproject ID: 544731). All data will be released before the publication of the manuscript.

### Field-specific reporting

Please select the one below that is the best fit for your research. If you are not sure, read the appropriate sections before making your selection.

- Life sciences       Behavioural & social sciences       Ecological, evolutionary & environmental sciences

## Life sciences study design

All studies must disclose on these points even when the disclosure is negative.

Sample size	No sample size calculation was performed; number of samples was determined based on the number of samples used in published bulk RNA-seq studies of MS and single-cell studies of pathological brain tissue from human patients, such as glioblastoma multiforme.
Data exclusions	No data were excluded.
Replication	The statistical model used for differential expression analysis included the individual label as a random-effect factor, thus identifying changes that are consistent across multiple MS patients. Findings based on snRNA-seq were independently validated using in situ RNA validation.
Randomization	Samples were segregated into experimental groups based on clinical diagnosis (MS or unaffected control).
Blinding	For quantification of cell numbers and RNA expression validation with in situ RNA hybridization, the operator and the person performing quantification was blinded to the sample labels.

## Reporting for specific materials, systems and methods

We require information from authors about some types of materials, experimental systems and methods used in many studies. Here, indicate whether each material, system or method listed is relevant to your study. If you are not sure if a list item applies to your research, read the appropriate section before selecting a response.

### Materials & experimental systems

n/a	Involved in the study
<input type="checkbox"/>	<input checked="" type="checkbox"/> Antibodies
<input checked="" type="checkbox"/>	<input type="checkbox"/> Eukaryotic cell lines
<input checked="" type="checkbox"/>	<input type="checkbox"/> Palaeontology
<input type="checkbox"/>	<input checked="" type="checkbox"/> Animals and other organisms
<input type="checkbox"/>	<input checked="" type="checkbox"/> Human research participants
<input checked="" type="checkbox"/>	<input type="checkbox"/> Clinical data

### Methods

n/a	Involved in the study
<input checked="" type="checkbox"/>	<input type="checkbox"/> ChIP-seq
<input checked="" type="checkbox"/>	<input type="checkbox"/> Flow cytometry
<input checked="" type="checkbox"/>	<input type="checkbox"/> MRI-based neuroimaging